Active site remodeling in IDH1 mutants drives distinct kinetic and potential resistance mechanisms

Matthew Mealka[1], Nicole A. Sierra[1], Diego Avellaneda Matteo[1], Elene Albekioni[1], Rachel Khoury[1], Timothy Mai[1], Brittany M. Conley[1], Nalani J. Coleman[1], Kaitlyn A. Sabo[1], Elizabeth A. Komives[2], Andrey A. Bobkov[3], Andrew L. Cooksy[1], Steve Silletti[2], Jamie M. Schiffer[4], Tom Huxford[1], and Christal D. Sohl[1,*]

[1]Department of Chemistry & Biochemistry, San Diego State University, San Diego, CA, USA
[2]Department of Chemistry & Biochemistry, University of California San Diego, La Jolla, CA, USA
[3]Sanford Burnham Prebys Medical Discovery Institute, La Jolla, CA USA
[4]Vividion Therapeutics, San Diego, CA, USA
*Corresponding author: Tel: +1 619-594-2039; E-mail: csohl@sdsu.edu

Enzyme mechanism, IDH1, structure-function relationships, HDX-MS, oncometabolite

Abstract

Human isocitrate dehydrogenase 1 (IDH1) is a highly conserved enzyme that converts isocitrate to α-ketoglutarate (αKG). IDH1 mutations affecting residue R132 drive tumor formation, and several FDA-approved mutant IDH1 inhibitors are available. Most mutants cannot catalyze the conventional reaction, but gain a neomorphic activity that produces D-2-hydroxyglutarate (D2HG). We previously reported that IDH1 R132Q uniquely preserves conventional activity while catalyzing robust D2HG production, allowing an opportunity to compare these reaction mechanisms within a single active site. Here, we employed static and dynamic structural methods and found that, compared to R132H, the R132Q active site adopted a conformation primed for catalysis with optimized substrate binding, hydride transfer, and prevention of inhibitor binding. When binding isocitrate, IDH1 R132Q exhibited a closed conformation with features consistent with decreased catalysis versus WT. Binding neomorphic reaction substrates resulted in semi-closure of IDH1 R132Q with profoundly limited active site solvent accessibility, and featured a distinct αKG binding pocket compared to R132H. This work enhances our understanding of fundamental IDH1 mechanisms while pinpointing regions that can improve inhibitor selectivity and drive resistance.

Introduction

Enzymes implicated in cancer usually employ one of two strategies: either increased or decreased catalytic activity that promotes a tumorigenic environment within the cell. Mutations in isocitrate dehydrogenase 1 (IDH1) can lead to an unusual third option –catalysis of a neomorphic reaction, the product of which drives

tumor formation. Wild type (WT) IDH1 is a highly conserved cytosolic and peroxisomal homodimeric enzyme that reversibly converts isocitrate (ICT) to α-ketoglutarate (αKG) in a $NADP^+$-dependent oxidative decarboxylation. However, tumor-driving IDH1 mutants catalyze the NADPH-dependent conversion of αKG to the oncometabolite D-2-hydroxyglutarate (D2HG), while also typically ablating the conventional reaction (Dang *et al*, 2009; Leonardi *et al*, 2012; Pietrak *et al*, 2011). The D2HG oncometabolite serves as a competitive inhibitor of αKG-dependent enzymes that include TET2, a 5-methylcytosine hydroxylase, and JmjC lysine demethylases to cause DNA and histone hypermethylation and cellular de-differentiation (Chowdhury *et al*, 2011; Figueroa *et al*, 2010). Mutations at residue R132 drive >85% lower grade and secondary gliomas (Dang *et al*, 2016) and ~40% of cartilaginous tumors (Cleven *et al*, 2017), with R132H and R132C mutations most common (Cerami *et al*, 2012; Gao *et al*, 2013). These mutated enzymes have been successfully therapeutically targeted, with several FDA-approved allosteric selective inhibitors currently in use and more in clinical trials (recently reviewed in (Adeva, 2022; Tangella *et al*, 2023; Sharma *et al*, 2023)).

While early kinetic characterization of the reaction catalyzed by IDH focused on bacterial forms, more recent efforts have been made to understand details of both WT and mutant catalysis by the human IDH1 enzyme. The conventional $NADP^+$-dependent conversion of ICT to αKG occurs via a random sequential mechanism (Rendina *et al*, 2013) with a measurable lag that can be eliminated via pre-incubation with the catalytic metal ion Mg^{2+} and ICT (Roman *et al*, 2019). As IDH1 WT binds its substrates, a major conformational change occurs where the large domain (residues 1-103 and 286-414, which includes the substrate binding pocket) and the small domain (residues 104-136 and 186-285) move towards each other relative to a hinge point (residues 134-141) in the clasp domain (residues 137-185) (Xu *et al*, 2004). This movement closes the active site cleft with a concomitant opening of a back cleft (Xu *et al*, 2004). A critical regulatory segment made up of the α10 helix (residues 271-285) helps to stabilize this open, inactive conformation (Xu *et al*, 2004). The α10 helix transitions from a coiled coil loop in the binary, cofactor-only-bound form (IDH1:NADP(H)) into a helix upon ICT binding, with this substrate replacing many of the interactions that had been made by the regulatory domain loop (Xu *et al*, 2004). In its helical form, this regulatory segment also helps properly orient the active site residues (Xu *et al*, 2004). Many features of the change from an open to a closed conformation were preserved during catalysis of the neomorphic reaction, with a crystallographic structure of R132H:NADP(H):αKG:Ca^{2+} (Rendina *et al*, 2013) superposing well on WT:NADP(H):ICT:Ca^{2+} (Xu *et al*, 2004), including the αKG substrate binding in the same location as the ICT substrate in the WT form (Xu *et al*, 2004). Curiously, a structure IDH1 R132H bound to ICT, which is not an effective substrate for this enzyme, showed significant differences both in the substrate binding site and in notable shifting of many features within the large and small domains (Yang *et al*, 2010).

These studies have established a foundation for understanding key kinetic and structural differences between IDH1 WT and one of the most common tumor-driving mutations, R132H. However, the IDH1 R132H mutant has low catalytic efficiency for D2HG production and a nearly negligible ability to drive the conventional reaction; inherent catalytic deficiencies with superior NADPH binding appear to allow this enzyme to eke out inefficient D2HG production though at great benefit to the tumor environment (Rendina *et al*, 2013; Dang *et al*, 2009; Pietrak *et al*, 2011). To better understand how D2HG production occurs, there is tremendous value in

studying a mutant that has more robust neomorphic reaction catalytic efficiency. Notably, IDH1 R132S/L/G/Q mutations have also been reported in patients with various frequencies (Bleeker *et al*, 2009; Balss *et al*, 2008; Borger *et al*, 2012; Mardis *et al*, 2009; Yan *et al*, 2009). Different mutations have also been shown to support distinct D2HG levels in tumors (Pusch *et al*, 2014). We have shown that these IDH1 mutants have unique kinetic properties for both neomorphic and conventional reactions (Avellaneda Matteo *et al*, 2017, 2018), and suggested that their unique kinetic features may explain at least some of the variability demonstrated in D2HG levels in patients (Avellaneda Matteo *et al*, 2018). In the course of our kinetic analyses, we identified one unusual mutant, IDH1 R132Q, that uniquely maintained IDH1 WT-like properties in that it retained some degree of conventional catalytic activity, but also drove unusually robust D2HG production (Avellaneda Matteo *et al*, 2017). This IDH1 R132Q mutant has been studied in mouse models, and has been shown to drive enchondroma tumor formation (Hirata *et al*, 2015).

Importantly, we also found that IDH1 R132Q was resistant to mutant IDH1 inhibitors (Avellaneda Matteo *et al*, 2018). We hypothesized that IDH1 R132Q must maintain sufficient WT-like features to sustain modest conventional reaction activity and resist interaction with inhibitors developed to target mutant IDH1, though it is not yet clear what kinetic or structural features drive these properties of this unusual mutant. A mechanistic understanding of IDH1 R132Q compared to both WT and R132H can help us identify additional selectivity handles for improved mutant IDH1 inhibitors. Further, as an H-to-Q mutation requires only a single point mutation, a secondary IDH1 H132Q mutation could represent a resistance strategy by conferring loss of inhibitor affinity while maintaining D2HG production. Investigating the atomic-level mechanisms that drive such diverse kinetic activity and inhibition among tumor-relevant IDH1 mutants can also inform the types of chemical features that can guide the field of enzyme design (Casadevall *et al*, 2023).

In this work, we sought to establish the static and dynamic structural features that drive the unique kinetic properties among tumor relevant IDH1 mutants, capitalizing on the unusual active site attributes that allow IDH1 R132Q to maintain both normal and neomorphic activities. We identified multiple conformations for IDH1 R132Q binding to the neomorphic substrate αKG, but not the conventional substrate ICT. Our kinetics and dynamic structural methods clarified that this ability of IDH1 R132Q to explore multiple conformations and substrate binding modes occurred within a relatively immobile, solvent-inaccessible enzyme that is better optimized for substrate binding, hydride transfer, and mutant IDH1 inhibitor resistance as compared to IDH1 R132H.

Results

Kinetic features of IDH1 R132Q suggest it is structurally optimized for substrate binding and hydride transfer steps relative to R132H.

We have previously demonstrated that IDH1 R132Q uniquely maintains modest catalytic efficiency for the conventional reaction (ICT to αKG conversion), while also displaying a much higher catalytic efficiency for the neomorphic reaction (αKG to D2HG conversion) relative to IDH1 R132H (Avellaneda Matteo *et al*, 2017, 2018). Steady-state kinetics analysis performed for this present study revealed a 5.6-fold increase in catalytic

efficiency for the conventional reaction in IDH1 R132Q compared to R132H, which was driven primarily by an 8.1-fold increase in k_{cat} (Fig. 1). The observed 9.4-fold increase in neomorphic reaction catalytic efficiency catalyzed by IDH1 R132Q compared to R132H resulted from a 3.5-fold increase in k_{cat} and 2.6-fold decrease in K_m (Fig 1). This suggests that features of IDH1 R132Q allow for improved transition state stabilization as well as providing more optimized on/off paths of the various reactants and products compared to R132H.

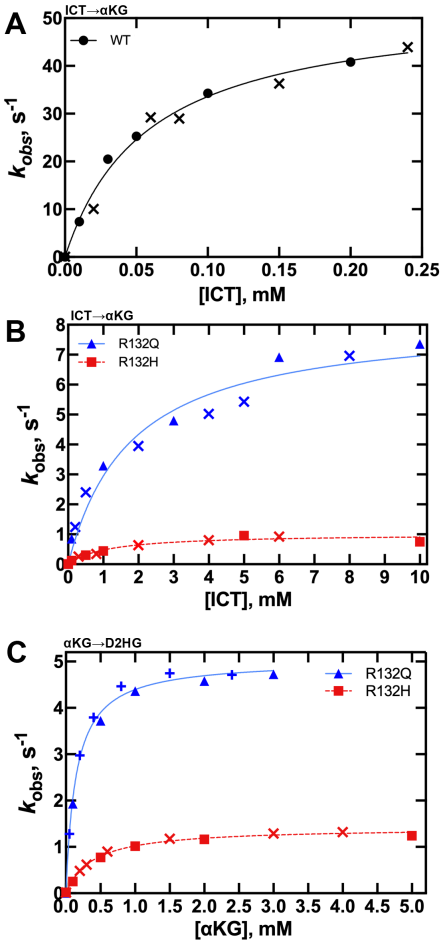

Figure 1. Steady-state kinetics analyses for IDH1 WT, R132Q, and R132H homodimers. *Steady-state kinetic parameters of the conventional reaction and the neomorphic reaction were measured as a function of varying substrate concentration. At least two protein preparations, indicated via different symbols, were used to measure the observed rate constants (k_{obs}), which were determined from the linear portion of plots of substrate concentration versus time. Each point in the curve represents a single replicate. A) The conventional reaction catalyzed by IDH1 WT yielded $k_{cat,\ ICT\rightarrow\alpha KG}$ = 53 ± 3 s^{-1}, $K_{M,\ ICT}$ = 0.058 ± 0.008 mM, and $k_{cat}/K_{M,\ ICT\rightarrow\alpha KG}$ 900 ± 100 $mM^{-1}s^{-1}$. B) The conventional reaction catalyzed by IDH1 R132Q (blue, $k_{cat,\ ICT\rightarrow\alpha KG}$ = 8.2 ± 0.6 s^{-1}, $K_{M,\ ICT}$ = 1.8 ± 0.4 mM, and $k_{cat}/K_{M,\ ICT\rightarrow\alpha KG}$ 5 ± 1 $mM^{-1}s^{-1}$) and by IDH1 R132H (red, $k_{cat,\ ICT\rightarrow\alpha KG}$ = 1.01 ± 0.07 s^{-1}, $K_{M,\ ICT}$ = 1.1 ± 0.3 mM, and $k_{cat}/K_{M,\ ICT\rightarrow\alpha KG}$ 0.9 ± 0.3 $mM^{-1}s^{-1}$). C) The neomorphic reaction catalyzed by IDH1 R132Q (blue, $k_{cat,\ \alpha KG\rightarrow D2HG}$ = 5.04 ± 0.07 s^{-1}, $K_{M,\ \alpha KG}$ = 0.15 ± 0.01 mM, and $k_{cat}/K_{M,\ \alpha KG\rightarrow D2HG}$ 34 ± 2 $mM^{-1}s^{-1}$) and by IDH1 R132H (red, $k_{cat,\ \alpha KG\rightarrow D2HG}$ = 1.42 ± 0.03 s^{-1}, $K_{M,\ \alpha KG}$ = 0.39 ± 0.03 mM, and $k_{cat}/K_{M,\ \alpha KG\rightarrow D2HG}$ 3.6 ± 0.3 $mM^{-1}s^{-1}$).*

Single-turnover, pre-steady-state kinetic experiments indicated that hydride transfer, or a step preceding it, was rate-limiting for the conventional reaction catalyzed by IDH1 WT and R132Q, as well as for the neomorphic reaction catalyzed by IDH1 R132Q and R132H (Fig 2). Interestingly, in single-turnover experiments for the neomorphic reaction by IDH1 R132H, treatment with lower concentrations of αKG showed

an initial lag in NADPH consumption that was eliminated upon using higher concentrations of αKG (Fig EV1). A lag in IDH-catalyzed reactions had been observed previously, suggestive of conformational changes induced by ICT and metal binding that drove the enzyme into its active state, and only pre-incubation with both ICT and metal was sufficient to eliminate the lag phase (Seery & Farrell, 1990; Roman *et al*, 2019; Herold *et al*, 2023; Farrell *et al*, 1990). Interestingly, this lag was not observed when the neomorphic reaction was catalyzed by IDH1 R132Q, despite using a concentration of αKG that was 10-fold lower than the concentration associated with a profound lag in IDH1 R132H (Figs 2D, EV1). This suggests that αKG is more proficient at driving IDH1 R132Q from an inactive to an active state compared to R132H, though it was not apparent through these experiments alone whether this was achieved by a more catalytically primed ground state or a faster conformational change.

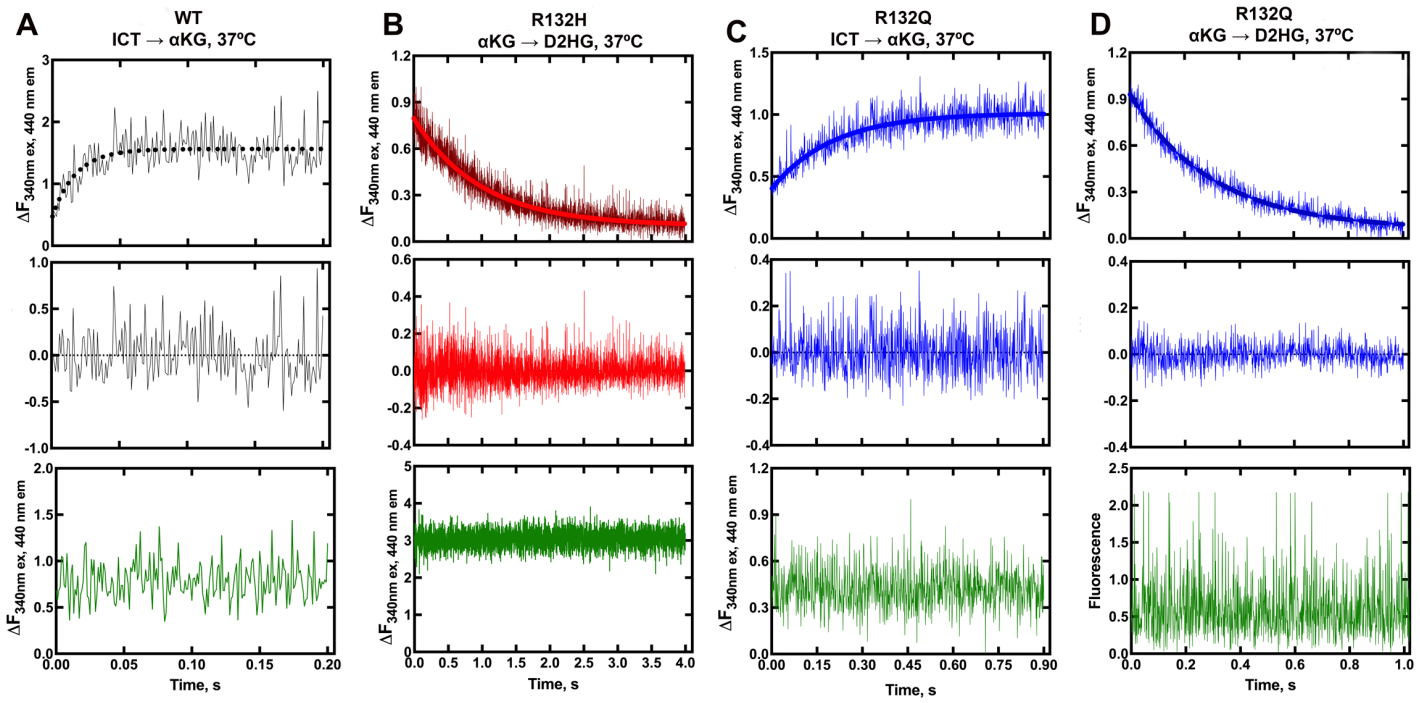

Figure 2. Pre-steady-state single-turnover kinetic features of IDH1 WT, R132H, and R132Q catalysis. *NADPH formation in the conventional reaction and consumption in the neomorphic reaction was monitored over the course of a single turnover (top plot) and compared with a control experiment lacking enzyme (bottom plot, in green). A single exponential equation ($Y = A_0e^{-kt}$) was fit to each experiment and residuals (middle plot) were obtained to assess goodness of fit. As this hydride transfer step rate matched our measured steady-state k_{cat} values, hydride transfer, or a step preceding it, is rate-limiting. A) Catalysis of the conventional reaction by IDH1 WT using 0.5 mM ICT, with a $k_{chem,\ ICT\rightarrow\alpha KG} = 58 \pm 10\ s^{-1}$. B) Catalysis of the neomorphic reaction by IDH1 R132H using 10 mM αKG to eliminate a lag, with a $k_{chem,\ \alpha KG\rightarrow D2HG} = 1.01 \pm 0.01\ s^{-1}$. C) Catalysis of the conventional reaction by IDH1 R132Q using 1 mM ICT, with a $k_{chem,\ ICT\rightarrow\alpha KG} = 4.9 \pm 0.2\ s^{-1}$. D) Catalysis of the neomorphic reaction by IDH1 R132Q using 0.5 mM αKG, with a $k_{chem,\ \alpha KG\rightarrow D2HG} = 3.27 \pm 0.06\ s^{-1}$.*

Unfortunately, we were unable to capture rates of conformational change by monitoring intrinsic protein fluorescence upon rapidly combining NADP(H) and substrate with IDH1 in the presence of Ca^{2+} to prevent turnover. However, we were able to measure rates of NADPH binding to IDH1 WT, R132H, and R132Q using enzyme that was stripped of cofactor (Rendina *et al*, 2013). We found that all three IDH1 proteins displayed single-step binding events, with an NADPH binding on rate (k_{on} or k_1) for IDH1 WT that was ~2-fold faster than that calculated for IDH1 R132Q, while k_{on} rates for IDH1 R132H were profoundly slower (Fig EV2). We also

used isothermal titration calorimetry (ITC) to measure equilibrium binding affinity of NADPH for IDH1. We found that both mutants exhibited a 5-fold decrease in K_d compared to IDH1 WT, suggesting a slower k_{off} rate resulted in the improved affinity for NADPH observed for IDH1 R132H despite the slow k_{on} rate (Fig EV2). Taken together, these kinetic data further supported the finding that when compared to R132H, IDH1 R132Q had a lower barrier to adopting the closed, active conformation that is driven by substrate and metal binding. To illuminate possible mechanisms behind these observations, we employed dynamic and static structural methods to elucidate the detailed features of IDH1 R132Q conformations in the absence and presence of substrates.

IDH1 R132Q has a less solvent accessible active site pocket that is more catalytically primed.

To expand our understanding of the time-resolved changes exhibited by IDH1 R132Q versus those in IDH1 WT and R132H, we first used HDX-MS analysis. We have previously demonstrated that IDH1 WT is amenable to this technique (Sabo *et al*, 2023). Here, we probed solvent accessibility as indicated by deuterium uptake in the binary IDH1:NADP(H) form, as WT and mutant IDH1 are known to copurify bound to NADP(H) (Roman *et al*, 2019; Herold *et al*, 2023). We also measured deuterium uptake upon the addition of substrate (ternary complex, IDH1:NADP(H):ICT/αKG), or upon the addition of substrate and Ca^{2+} (quaternary complex, IDH1:NADP(H):ICT/αKG:Ca^{2+}). HDX-MS analysis again proved highly suitable to assess global IDH1 WT, R132H, and R132Q dynamics, with 99.8% coverage with 112 total peptides and 4.12 redundancy. By far the most substantial change in deuterium uptake for IDH1 WT, R132H, and R132Q occurred upon binding substrates and the metal cation in the quaternary form, indicative of closed, catalytically competent conformations among all enzyme species (Fig EV4). This is consistent with previous findings that both substrate (ICT, but also presumably αKG in the neomorphic reaction) and divalent metal binding are required to drive IDH1 into its fully closed, active conformation (Seery & Farrell, 1990; Roman *et al*, 2019; Herold *et al*, 2023; Farrell *et al*, 1990). In general, deuterium uptake was lowest overall in R132Q:NADPH:αKG:Ca^{2+}, followed by R132Q:NADPH:ICT:Ca^{2+} and then WT:$NADP^+$:ICT:Ca^{2+}, while R132H:NADPH:αKG:Ca^{2+} exhibited by far the most deuterium uptake (Figs 3, EV4, EV5). The observed decreased solvent uptake by IDH1 R132Q suggests an overall less structurally dynamic, more closed conformation compared to R132H.

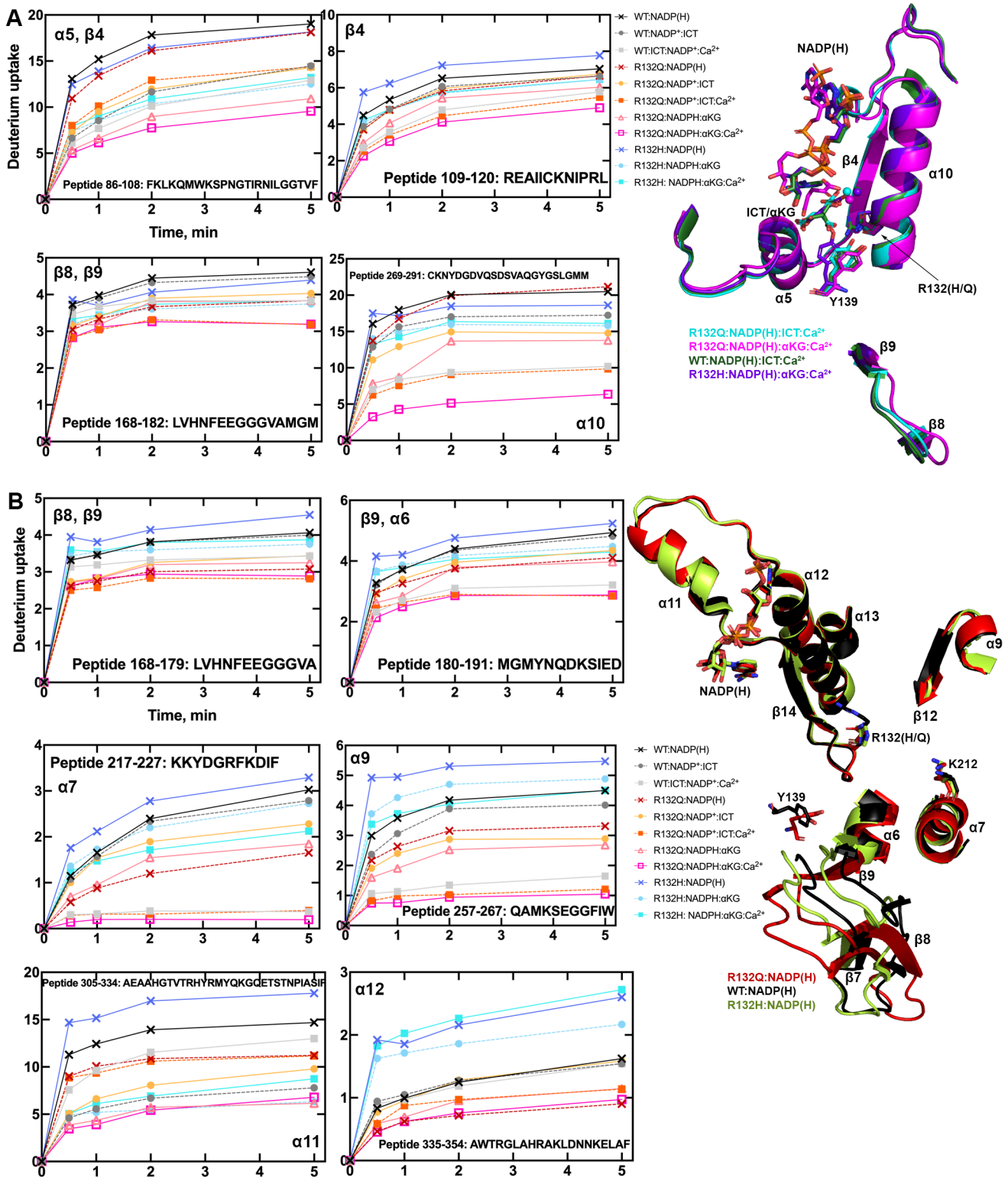

Figure 3. IDH1 R132Q has lower deuterium uptake than R132H in both binary and quaternary complexes. *A) Peptides comprised of residues 86-123, 168-209, and 260-291 showed very low deuterium uptake for substrate-bound IDH1 R132Q relative to R132H, with representative deuterium uptake plots indicated on the left. The structural features of IDH1 R132Q, WT (Xu et al, 2004), and R132H (Rendina et al, 2013) encompassing these peptides are shown in cartoon (right). B) Peptides comprised of 144-191, 217-227, 257-267, and 295-354 showed notably low deuterium uptake for NADP(H)-only-bound IDH1 relative to R132H, with representative deuterium uptake plots shown on the left. The structural features of IDH1 R132Q, WT (Xu et al, 2004), and R132H (Yang et al, 2010) encompassing these regions are shown in cartoon (right). Secondary structures associated with the peptides are indicated.*

Based on our kinetic studies suggesting IDH1 R132Q had a lower barrier to achieve the active, fully closed conformation compared to R132H, we predicted that the R132Q:NADP(H) complex may experience less deuterium uptake compared to the R132H binary form since R132Q would be in a more quaternary-like state. Unsurprisingly, in general, the IDH1:NADP(H) binary forms of all three proteins showed overall high deuterium uptake, particularly among residues 55-104 (α3/β3/α4/α5), 190-204 (α6), 237-271 (α8/β11/α9/β12/α10), and 365-376 (parts of α13/α14) (Figs 3, EV4, EV5). Many of these regions encompass the NADP(H) binding site, which is made up primarily by residues 74-93 that include the α4 helix, and residues 307-325 that contain the α11 helix (Fig 4). As predicted, R132Q:NADP(H) and WT:NADP(H) had the least deuterium uptake overall, while R132H:NADP(H) exhibited, by far, the most uptake (Figs 3, EV4, EV5). In particular, regions at the NADP(H) binding pocket including the α9, α11, and α12 helices and the β13/β14 strands all showed lower deuterium uptake for R132Q:NADP(H) relative to R132H:NADP(H) (Fig 3). This trend of lower uptake by binary IDH1 R132Q compared to R132H was also observed in the protein stabilizing regions of the clasp domain (β8/β9 and α6) and the dimer interface (α7) (Fig 3). Notably, the WT:NADP(H) binary condition behaved like R132Q in these regions, with much lower deuterium uptake compared to R132H, consistent with a more primed, catalytically-ready conformation relative to IDH1 R132H. However, there was one notable deviation in this trend: peptides encompassing the α1 helix had the highest deuterium uptake for IDH1 R132Q (Figs 4, EV4, EV5). In all three binary conditions the deuterium uptake decreased at the *C*-terminal end of the α1 helix, with IDH1 R132Q maintaining more deuterium uptake in the *N*-terminal portion of this helix (Fig EV5). However, overall, our HDX-MS and kinetics data suggest that NADP(H)-bound IDH1 R132Q has a more closed/less mobile conformation that is in a more catalytically competent state compared to IDH1 R132H.

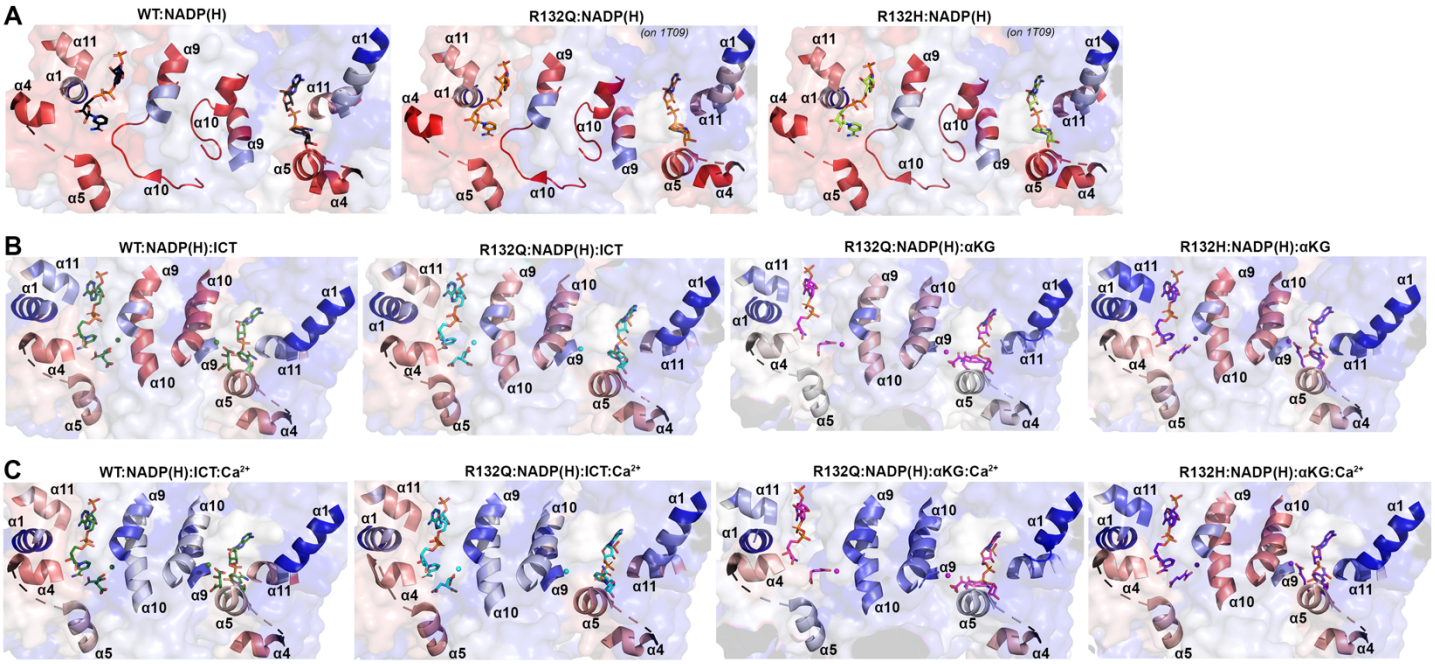

Figure 4. Deuterium uptake by IDH1 WT, R132Q, and R132H in helices bounding the substrate binding pocket. *Deuterium uptake is shown as a gradient from red (high uptake) to blue (low uptake). A) Deuterium uptake by IDH1 WT, R132Q, and R132H upon no ligand treatment. These HDX-MS data were overlaid on NADP(H)-only bound forms of WT* (Xu *et al*, 2004) *in all three cases, as the αKG helix was disordered in the NADP(H)-only bound forms of IDH1 R132Q and R132H* (Yang *et al*, 2010)*. B) Deuterium uptake by WT and*

R132Q upon treatment with NADP$^+$ and ICT, and by IDH1 R132Q and R132H upon treatment with NADPH and αKG. These HDX-MS data were overlaid on WT:NADP(H):ICT:Ca^{2+} (Xu *et al*, 2004)*, R132Q:NADP(H):ICT:Ca^{2+} and R132Q:NADP(H):αKG:Ca^{2+}, or R132H:NADP(H): αKG:Ca^{2+}* (Rendina *et al*, 2013)*. C) Deuterium uptake by IDH1 WT and R132Q upon treatment with NADP$^+$, ICT, and Ca^{2+}, and by IDH1 R132Q and R132H upon treatment with NADPH, αKG, and Ca^{2+}. These HDX-MS data were overlaid on the structures described in (B).*

Since the substrate binding regions generally showed lower deuterium uptake in the R132Q:NADP(H) condition compared to R132H, we wondered if the temporal features of our HDX-MS data suggested a faster closing upon substrate binding. This would provide one mechanism of the improved catalytic efficiency shown by IDH1 R132Q relative to R132H in both the conventional and neomorphic reactions. To address this, we inspected peptides that included residues within 4 Å of the bound NADP(H) and ICT/αKG substrates to determine if deuterium uptake equilibrium was reached faster in IDH1 R132Q versus R132H, consistent with a primed ground state that reached a closed conformation more easily. Interestingly, the peptides that contained active site residues from the adjacent monomer (i.e., chain B residues contributing to the chain A active site, residues K212', T214', L250', D252', D253', Q257', and K260') showed a faster approach to deuterium uptake equilibration for IDH1 R132Q and WT compared to R132H (Fig EV6). Specifically, peptide 240-253 reached equilibrium by 2 min for ICT-bound R132Q and WT and for αKG-bound R132Q conditions, while αKG-bound R132H appeared to not yet reach equilibrium. Peptide 257-267 rapidly reached equilibrium in both ICT- and αKG-bound R132Q conditions, likely in part due to very limited deuterium uptake overall in this region. This is in contrast to a much slower approach to equilibrium by R132H and, to a lesser degree, WT. Peptide 210-216 showed ICT-bound R132Q reaching equilibrium by ~1 min, while ICT-bound WT and αKG-bound R132Q and αKG-bound R132H reached uptake equilibrium at 2 min. Overall, these data support the hypothesis that the ground state of IDH1 R132Q is a more closed conformation that follows a simpler path to a catalytically competent state compared to R132H.

HDX-MS analyses are valuable to predict dynamic features of proteins upon substrate binding, and ideally these dynamic, intermediate-resolution data are paired with static, high-resolution X-ray crystal structures. Here we report the first X-ray crystal structures of IDH1 R132Q. Overall, we refined six new crystallographic models: two structures of a binary form of IDH1 R132Q bound to NADP(H) (R132Q:NADP(H), PDB ID 8VHC and 8VH9); one structure of R132Q bound to the conventional reaction substrates in the presence of a calcium ion that mimics the catalytic Mg^{2+} (R132Q:NADP(H):ICT:Ca^{2+}, PDB ID 8VHD); two structures of R132Q bound to the neomorphic reaction substrates in the presence of a calcium ion (R132Q:NADP(H):αKG:Ca^{2+}, PDB ID 8VHB and 8VHA), and one structure of R132Q bound to a NADP-TCEP adduct in the presence of a calcium ion (R132Q:NADP-TCEP:Ca^{2+}, PDB ID 8VHE). These structures facilitated comparisons with previously solved IDH1 WT (Xu *et al*, 2004) and R132H structures (Rendina *et al*, 2013; Yang *et al*, 2010), including comparisons among binary, ICT-bound quaternary (conventional reaction substrates), and αKG-bound quaternary (neomorphic reaction substrates) structures of WT, R132Q, and R132H.

The binary structures of IDH1 R132Q (R132Q:NADP(H)) were valuable to help us better understand how the active sites of cofactor-bound IDH1 R132Q compared to R132H. We describe here two structures

crystalized in either sulfate (8VHC) or citrate (8VH9) (Fig. 5). Though both forms aligned very well and appeared otherwise identical, we feared the citrate buffer could nonetheless promote more substrate-bound-like features due to its structural similarity to isocitrate. Thus, the binary structure crystallized in sulfate was used for all further comparisons and alignments. We noted both forms contained a glycerol molecule near the NADP(H) binding site in both molecules, away from the ICT/αKG binding pocket. While the R132Q binary complex showed no major global structural alterations upon dimer alignment with previously solved structures of WT:NADP(H) (Xu *et al*, 2004) and R132H:NADP(H) (Yang *et al*, 2010), many local shifts were observed (Fig 5). Unsurprisingly, both NADP(H)-bound IDH1 R132Q structures showed the typical overall open, inactive conformation seen in IDH1 WT and R132H, with larger active site clefts (by convention, measured as the distance between residues 76 in chain A and 250' in chain B) and smaller back clefts (measured as the distance between residues 199 to 342 in chain A) relative to the quaternary, substrate- and metal ion-bound forms (Table 1). Interestingly, these distances in the binary IDH1 R132Q structure more closely resembled binary IDH1 WT than binary IDH1 R132H, in further support of a more closed, catalytically competent ground state for R132Q. Despite these WT-like features, in dimer-based alignments of the crystal structures, IDH1 R132Q exhibited notable differences from both WT and R132H. In particular, the clasp domain and helices proximal to the substrate and cofactor binding site revealed deviations, particularly in the *C*-terminus of the α1 helix and the α2, α4, α5, and α11 helices, which were shifted upwards and inwards in IDH1 R132Q versus WT and R132H binary complexes, resulting in a similar shift of the NADP(H) molecule itself (Fig 5B). Indeed, this inward shifting of the α1 helix is an important feature of the closed, catalytically competent conformation. IDH1 R132Q also maintained an extensive hydrogen bonding network enveloping the NADP(H) molecule; this network was far less robust in IDH1 R132H (Fig EV7).

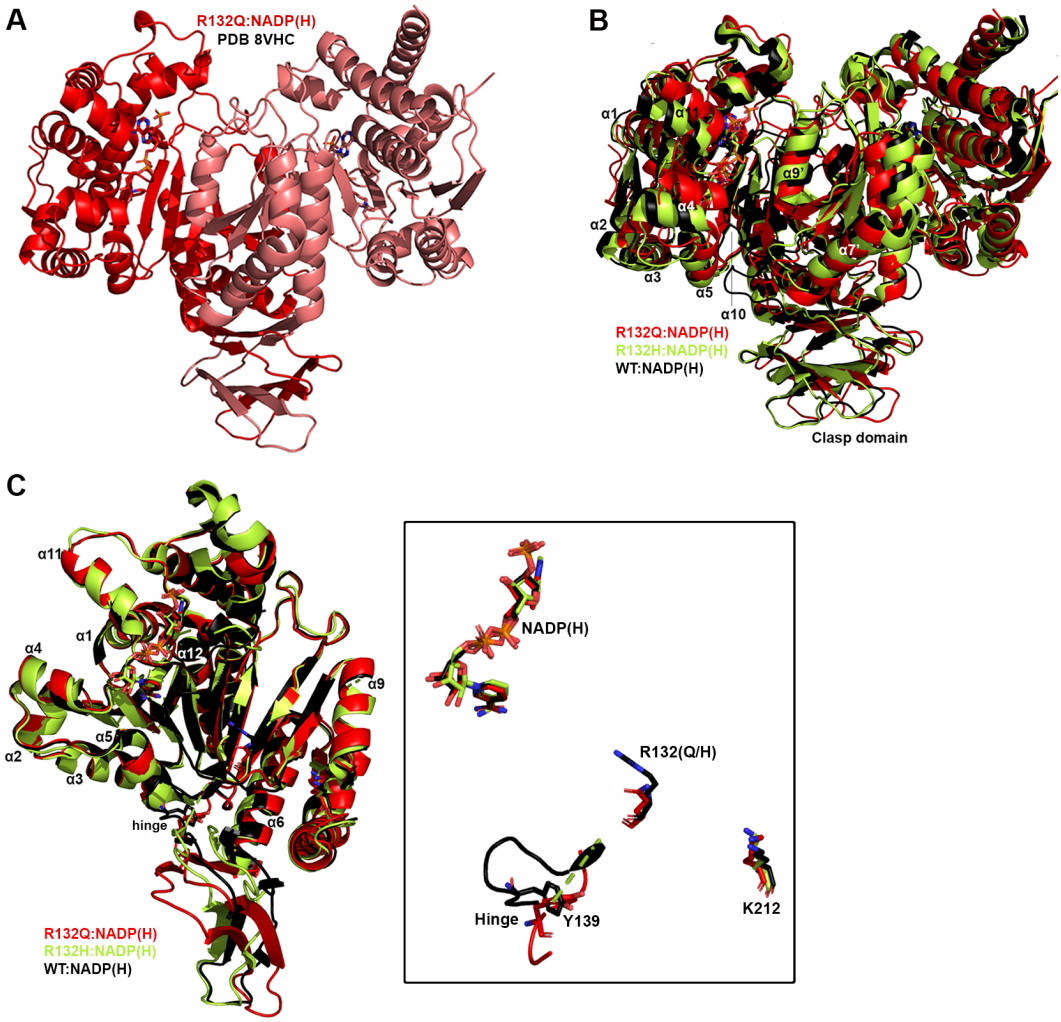

Figure 5. Crystal structure of cofactor-only-bound IDH1 R132Q. *A) The binary complex of IDH1 R132Q bound to NADP(H) is found in an open, catalytically inactive conformation. Each R132Q monomer is highlighted using a slight change in color. B) The R132Q:NADP(H) dimer (8VHC) is shown aligned to WT:NADP(H) (1T09* (Xu *et al*, 2004)*) and R132H:NADP(H) (3MAR* (Yang *et al*, 2010)*). C) Monomer-based alignments are shown with R132Q:NADP(H), WT:NADP(H)* (Xu *et al*, 2004) *and R132H:NADP(H)* (Yang *et al*, 2010)*). These alignments were used to feature the overall secondary structure, as well as the catalytic residues (Y139 and K212, though the latter residue drives catalysis in the monomer not shown), residue R132(H/Q), and the cofactor (shown in inset).*

Table 1. Active site and back cleft measurements assessing open versus closed conformations.

PDB ID	IDH1 complex (monomer/monomer listed if applicable)	I76 to L250' active site cleft distance, Å	I76' to L250 active site cleft distance, Å	M199 to H342 back cleft distance, Å	M199' to H342' back cleft distance, Å
8VHC	R132Q:NADP(H) [a]	14.7	16.9	9.1	8.9
8VH9	R132Q:NADP(H) [b]	14.2	17.1	8.7	8.4
8VHD	R132Q:NADP(H):ICT:Ca^{2+}/ R132Q:NADP(H):Ca^{2+}	8.8 (ICT)[c]	10.4 (no ICT)	10.1 (ICT)	10.3 (no ICT)
8VHB	R132Q:NADP(H):αKG:Ca^{2+}/ R132Q:NADP-αKG:Ca^{2+}	10.6 (αKG)	11.7 (adduct)	9.8 (αKG)	9.5 (adduct)
8VHA	R132Q:NADP(H):αKG:Ca^{2+}/ R132Q:NADP-αKG:Ca^{2+}	11.3 (αKG)	12.2 (adduct)	10.2 (αKG)	10.0 (adduct)
8VHA	R132Q:NADP-αKG:Ca^{2+}/ R132Q:NADP(H):Ca^{2+}	8.7 (adduct)	11.8 (no αKG)	9.7 (adduct)	10.6 (no αKG)
8VHE	R132Q:NADP-TCEP: Ca^{2+}	11.8	11.3	9.6	10.7
1T09[d]	WT:NADP(H)	17.6	14.8	8.3	9.0

1T0L[d]	WT:NADP(H):ICT:Ca^{2+}	8.8	8.6	11.1	11.1
4L03[e]	G97D:NADP(H):αKG:Ca^{2+}	8.6	8.7	10.9	11.1
3MAR[f]	R132H:NADP(H)	17.8	15.1	8.3	8.4
3MAP[f]	R132H:NADP(H):ICT	16.1	14.1	7.7	8.0
4KZO[e]	R132H:NADP(H):αKG:Ca^{2+}	8.4	8.6	10.9	11.1

[a] Condition crystallized in sulfate
[b] Condition crystallized in citrate
[c] Dimers containing monomers with different molecules in the active site are indicated in the second column, and measurements associated with each monomer are identified by listing the active site molecule present in parenthesis.
[d] (Xu *et al*, 2004)
[e] (Rendina *et al*, 2013)
[f] (Yang *et al*, 2010)

Monomer-based alignments of the binary structures of R132Q with IDH1 WT and R132H also showed prominent deviations in the clasp domain, which plays a major role in maintaining the dimer. Notably, IDH1 R132Q contained the longest, most intact β strands in the clasp domain, while only the β7 strand was fully intact in IDH1 R132H while the remaining clasp features were loops (Fig 5). Cofactor-only-bound IDH1 WT also exhibited less structural order in this region, with two loops bookended by very short β strands. In contrast to both IDH1 R132H and WT, the IDH1 R132Q binary form had fully intact β7 and β8 strands in the clasp domain, with peptides in the β8 strand of R132Q:NADP(H) displaying low deuterium uptake (Figs 3B and EV5) in contrast to higher uptake in WT:NADP(H) and the highest uptake in R132H:NADP(H). In addition to more organized secondary structure features, β strands and loops in the clasp were shifted to one side for the R132Q:NADP(H) complex compared to WT and R132H binary forms (Fig 5). Importantly, consistent with kinetic and HDX-MS data suggesting a more catalytically primed state for R132Q:NADP(H), these intact β strands in the binary R132Q complex were reminiscent of quaternary, fully substrate-bound forms of IDH1 WT and R132Q (*vide infra*). Together, both dynamic and static structural data suggest that the IDH1 R132Q active site pocket and surrounding features have greater rigidity and more defined structural features typical of fully-substrate-bound forms of IDH1, suggesting that R132Q:NADP(H) is better predisposed for catalytic activity compared to IDH1 R132H.

IDH1 R132Q maintains a typical closed conformation in its ICT-bound form similar to WT, with features that suggest decreased catalytic efficiency.

Here, we also report the first ICT-bound quaternary structure of IDH1 R132Q (R132Q:NADP(H):ICT:Ca^{2+}, 8VHD, Fig 6). In both dimer-based (Figs 6B) and monomer-based (Fig 6C) alignments of R132Q:NADP(H):ICT:Ca^{2+} with WT:NADP(H):ICT:Ca^{2+} (Xu *et al*, 2004), there was obvious overlap not only in global features, but also excellent alignment of active site details, including location of substrates, metal ion, and catalytic residues. Interestingly, ICT-bound IDH1 R132Q also aligned well with R132H bound to its preferred substrate, αKG (R132H:NADP(H):αKG:Ca^{2+}) (Rendina *et al*, 2013). Like ICT-bound WT and αKG-bound R132H structures, conventional substrate-bound IDH1 R132Q adopted a catalytically competent, closed conformation, with ICT maintaining many of the same polar interactions with the protein and divalent ion as observed with IDH1 WT, supportive of our kinetic data showing measurable ICT to αKG conversion by R132Q.

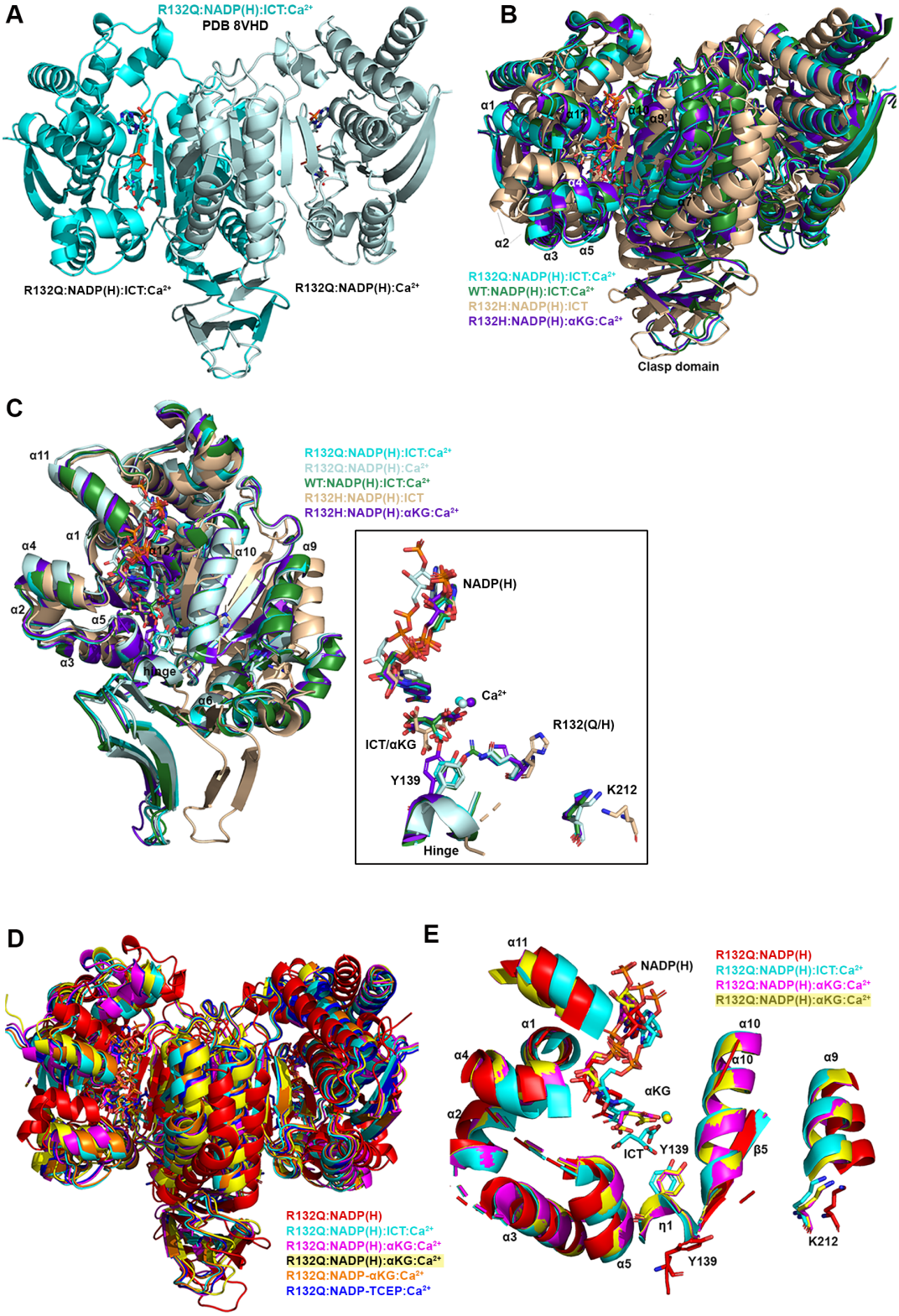

Figure 6. Crystal structure of IDH1 R132Q bound to ICT, NADP(H) and Ca^{2+}. *A) The quaternary R132Q:NADP(H):ICT:Ca^{2+} complex is shown in a catalytically closed, active conformation, despite the presence of ICT in only the left monomer. Each R132Q monomer is highlighted using a slight change in color. B) Here, dimer-based alignments comparing IDH1 R132Q, R132H, and WT are shown. The dimer made up of R132Q:NADP(H):ICT:Ca^{2+} (on left) and R132Q:NADP(H):Ca^{2+} monomers (on right) is shown in cyan (8VHD); R132H:NADP(H):ICT is in wheat (3MAP (Yang et al, 2010)); R132H:NADP(H):αKG:Ca^{2+} is in dark purple (4KZO (Rendina et al, 2013)); and WT:NADP(H):ICT:Ca^{2+} is in dark green (1T0L (Xu et al, 2004)). C) Monomer-based alignments of primarily ICT-containing monomers are shown. Of the ICT-bound IDH1 R132Q dimer, the R132Q:NADP(H):ICT:Ca^{2+} monomer is in dark cyan and the R132Q:NADP(H):Ca^{2+} monomer is in*

light cyan. For clarity, monomer-based alignments of only the catalytic residues, residue R132X, cofactor, substrates, Ca^{2+} and hinge are shown in the inset. D) A dimer-based alignment of R132Q:NADP(H), R132Q:NADP(H):ICT:Ca^{2+}, and R132Q:NADP(H):αKG:Ca^{2+}. E) A monomer-based alignment of the IDH1 R132Q structures described in (D) with substrates, catalytic residues, and nearby secondary structure features highlighted.

Even though alignment of ICT-bound IDH1 WT and R132Q was strikingly similar, the notable 180-fold decrease in catalytic efficiency (Fig 1) suggested that maintaining hydrogen bonding features and active site structuring was not fully sufficient for robust conventional activity in R132Q. One notable difference in the ICT-bound IDH1 R132Q and WT structures was the lack of ICT in one monomer in the R132Q:NADP(H):ICT:Ca^{2+} complex (Fig 6). As a result, NADP(H) in the ICT-absent R132Q monomer was shifted slightly upward and outward due to, at least in part, a similar upward and outward shift in the α11 helix (Fig 6), reminiscent of the WT:NADP(H) binary structure (Fig 6). While the R132Q:NADP(H):ICT:Ca^{2+} monomer maintained an active site cleft distance similar to that of the quaternary WT conformation indicative of a fully closed, catalytically competent conformation, the back cleft was not quite as open as either IDH1 WT or R132H quaternary complexes (Table 1). However, either Ca^{2+} binding and/or the presence of ICT in the adjacent monomer still affected the R132Q:NADP(H):Ca^{2+} monomer; though its measurements indicated a slightly more open active site cleft and closed back cleft, it still more closely resembled the substrate-bound forms rather than the binary complexes (Table 1). The importance of the divalent metal on the ICT-bound IDH1 R132Q active site was supported by our HDX-MS data. Though ICT- and ICT and Ca^{2+}-bound IDH1 R132Q generally had similar deuterium uptake features to IDH1 WT, both the ternary and quaternary ICT-containing conditions for R132Q had higher uptake than the corresponding αKG-containing conditions for this protein (Figs 3, 4). This feature of ICT-bound IDH1 R132Q being more solvent accessible than the αKG-bound form contrasts with the structural measurements indicating a more open conformation for the αKG-bound quaternary complex of IDH1 R132Q (Table 1, *vide infra*). This suggests that simple static measurements of open versus closed clefts are not sufficient to capture the complex dynamics associated with substrate binding.

This lack of active site saturation suggested a lower affinity toward ICT for IDH1 R132Q versus WT. Though K_m values are not affinity measurements, it is noteworthy that there was a >300-fold increase in this parameter when comparing IDH1 R132Q to WT. To better address differences in binding affinity among IDH1 WT, R132Q, and R132H, we again turned to ITC experiments. While ICT binding affinity for IDH1 R132H was below the limit of detection, we found that IDH1 R132Q indeed exhibited a ~170-fold decrease in ICT affinity compared to WT (1000 ± 300 μM vs 5.8 ± 0.9 μM, Fig EV3). This loss of affinity for ICT by R132H versus R132Q was readily explained by a comparison of ICT-bound structures of these two mutants. ICT binding to IDH1 R132Q was supported by extensive polar contacts, including hydrogen bonding to catalytic residue Y139 (Fig EV7). This was in sharp contrast to the limited polar interactions experienced by ICT when bound to IDH1 R132H (Yang *et al*, 2010) (Fig EV7). Differences in ICT binding in IDH1 R132Q versus R132H were not solely limited to hydrogen bonding features; instead, there were profound global structural differences as well. In the ternary R132H:NADP(H):ICT structure that had “quasi-open” monomers, ICT was found in a posited pre-binding site that was shifted to the left of the site associated with a fully active (closed) conformation (Yang *et*

al, 2010). While the IDH1 R132Q ICT-bound structure had catalytic residues that were oriented in a kinetically competent conformation, in the R132H ICT-bound structure, these residues were swung away from the active site, akin to positioning found in cofactor only-bound, catalytically incompetent IDH1 structures (Table 1, Fig 6B, 6C). This conformation adopted by R132H:NADP(H):ICT was facilitated at least in part by a shift of the α4 and α11 helices upwards and outwards away from the dimer interface, and an unraveling of the α10 helix; all regions we and others have shown previously as being highly flexible (Xu *et al*, 2004; Yang *et al*, 2010; Chambers *et al*, 2020; Sabo *et al*, 2023). Though this IDH1 R132H structure did not include a divalent metal that may be required for full closure, it is nonetheless unsurprising that IDH1 R132H, in contrast to IDH1 R132Q, is essentially unable to convert ICT to αKG.

IDH1 R132Q αKG-bound form is semi-closed, with an αKG binding pocket that is unique from R132H.

Since IDH1 R132Q uniquely maintains both normal and neomorphic catalytic abilities, we wondered how the binding conformations for ICT, the conventional reaction substrate, and αKG, the neomorphic reaction substrate, compared. Here, we report two αKG-containing IDH1 R132Q quaternary structures (R132Q:NADP(H):αKG:Ca^{2+}, 8VHA and 8VHB) (Fig 7). Surprisingly, co-crystallization of IDH1 R132Q with NADPH, αKG, and Ca^{2+} led to a variety of complexes, with monomer asymmetry still observed. One structure had αKG, NADP(H), and Ca^{2+} bound in one monomer, and a covalent NADP-αKG adduct and Ca^{2+} in the other (8VHB, Fig 7A). Cleft measurements in both monomers indicated a slightly more open conformation when compared to the closed quaternary R132Q (ICT-bound), WT (ICT-bound) and R132H (αKG-bound) structures, with the α11 helix shifted out away slightly from the substrate binding pocket (Fig 7E). As a result, the NADP(H) itself shifted outwards compared to the ICT-bound R132Q structure. However, this conformation was not nearly as open as the cofactor only-bound forms (Table 1). Thus, both monomers in this IDH1 R132Q dimer are in a semi-closed conformation, with the αKG-containing monomer slightly more closed than the adduct-containing monomer.

The second αKG-bound structure (8VHA) had unique features among two dimers in the crystallographic asymmetric unit. One catalytic dimer also contained one monomer with an NADP-αKG adduct and one monomer with an αKG molecule (Fig 7B), similar to the 8VHB structure. However, this dimer had a more open active site cleft with similar back cleft distances, though the αKG-containing monomer still had more closed-like features than the adduct-containing monomer (Table 1). Again, this dimer appeared as an intermediate between the R132Q:NADP(H) and the R132Q:NADP(H):ICT:Ca^{2+} structures, with, for example, the intact α10 helix, the α2, α5, and α11 helices, and hinge/η1 aligning well with the fully closed ICT-bound quaternary IDH1 R132Q structure, but the α1 and α4 helices and NADP(H) molecule aligning better with the binary R132Q:NADP(H) (Fig 6E). A second dimer contained an NADP-αKG adduct and Ca^{2+} in one monomer and only NADP(H) and Ca^{2+} in the other (Fig 7C). Interestingly, this dimer appeared to be in a more closed, catalytically competent conformation, reminiscent of the fully closed WT quaternary structure (Table 1). The Ca^{2+} ion clearly led to extensive restructuring, as the R132Q:NADP(H):Ca^{2+} monomer aligned relatively poorly with the R132Q:NADP(H) complex despite the only difference being the presence of the metal ion (Fig 7H). Thus, closing of IDH1 R132Q to the αKG-bound form may be driven just as much by metal binding as by

substrate binding. This finding was recapitulated upon noting the differences in overall deuterium uptake when comparing R132Q:NADPH:αKG-treated and R132Q:NADPH:αKG:Ca^{2+}-treated forms, which were mostly associated with decreased deuterium uptake in β4 through β5 including the intervening loop, the loop between β10 and α7, part of the α7 helix, α9, and α10 (Figs 3, EV5, EV6). Thus, we have captured snapshots of stable conformations of αKG binding ranging from semi-closed (αKG-bound) to essentially fully closed (NADP-αKG adduct-bound).

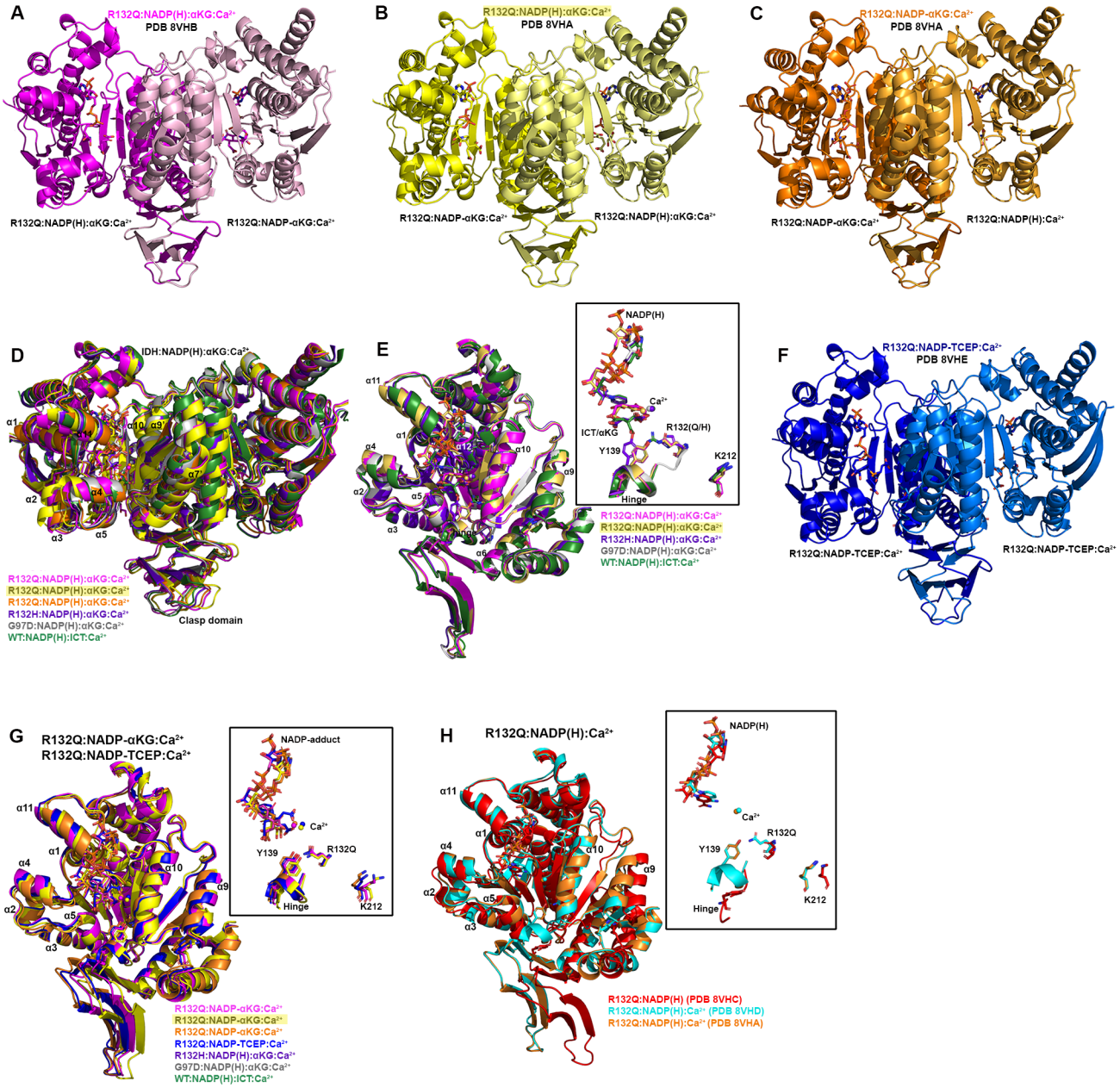

Figure 7. Crystal structure of IDH1 R132Q bound to αKG and NADP-adducts. *In (A-C) and (F), each R132Q monomer is highlighted using a slight change in color. A) A quaternary complex of R132Q bound to NADP(H), αKG, and Ca^{2+} in one monomer, and a NADP-αKG adduct and Ca^{2+} in the other monomer is shown (8VHB). B, C) A second quaternary complex (8VHA) with two unique dimers containing either one R132Q:NADP-αKG:Ca^{2+} monomer and one R132Q:NADP(H):αKG:Ca^{2+} monomer in (B), or one R132Q:NADP-αKG:Ca^{2+} monomer and one R132Q:NADP(H):Ca^{2+} monomer in (C). D) Dimer-based alignments of R123Q αKG-bound structures are shown in comparison to R132H:NADP(H):αKG:Ca^{2+}* (Rendina *et al*, 2013)*, G97D:NADP(H):αKG:Ca^{2+} (4L03* (Rendina *et al*, 2013)*), and WT:NADP(H):ICT:Ca^{2+}* (Xu *et al*, 2004)*. E) Monomer-based alignment of αKG-containing R132Q monomers with R132H:NADP(H):αKG:Ca^{2+},*

WT:NADP(H):ICT:Ca^{2+}, and G97D:NADP(H):αKG:Ca^{2+}. F) A structure of R132Q bound to Ca^{2+} and a NADP-TCEP adduct present in both monomers. G) Alignment of adduct-containing IDH1 R132Q monomers. H) Alignment of IDH1 R132Q monomers lacking ICT or αKG. R132Q:NADP(H) is in red, the non-ICT-containing R132Q monomer (R132Q:NADP(H):Ca^{2+}, which dimerizes with a R132Q:NADP(H):ICT:Ca^{2+} monomer) is in cyan, and the non-αKG-containing R132Q monomer (R132Q:NADP(H):Ca^{2+}, which dimerizes with a R132Q:NADP(H):αKG:Ca^{2+} monomer) is in orange.

Closed conformations are seen in WT and R132H IDH1 when bound with their preferred substrates (ICT for WT and αKG for R132H), with the structures of WT:NADP(H):ICT:Ca^{2+} (Xu *et al*, 2004) and R132H:NADP(H):αKG:Ca^{2+} (Rendina *et al*, 2013) monomers aligning well (Fig 7). After finding that the conformation of the αKG-bound R132Q was often not as fully closed as the ICT-bound form, we also wondered how αKG-bound R132Q compared to these WT and R132H closed conformations. In alignments of R132Q:NADP(H):αKG:Ca^{2+} with the WT and R132H quaternary structures (7D, 7E), the catalytic residue Y139 in IDH1 R132Q was shifted away from the αKG molecule. The αKG molecule also made far fewer hydrogen bond contacts within the IDH1 R132Q active site as compared to R132H (Fig EV7). In IDH1 R132Q, the αKG binding site itself was shifted upwards towards NADP(H) and away from the substrate binding sites seen in the WT:NADP(H):ICT:Ca^{2+} and R132H:NADP(H):αKG:Ca^{2+} structures. This shift upward of αKG towards NADP(H) might be facilitated by one surprising feature of all non-αKG-containing monomers -- the nicotinamide ring could not be reliably modeled due to missing electron density. This suggests that when αKG was absent (such as in the R132Q:NADPH:Ca^{2+} monomer that dimerized with the NADPH-αKG adduct) or, more unexpectedly, when αKG was bound (R132Q:NADPH:αKG:Ca^{2+} monomers), this portion of NADP(H) was more dynamic in the active site (Fig 7G, 7H). Overall, the αKG-containing structures of IDH1 R132Q either did not appear in a catalytically-ready form, or its enzymatic mechanism may rely more heavily on different amino acids for steps in acid-base chemistry than are used in the conventional reaction.

Unique static and dynamic structural features are associated with ICT versus αKG binding to IDH1 R132Q.

The catalytic efficiency of the neomorphic reaction (αKG to D2HG) catalyzed by IDH1 R132Q was ~7-fold higher compared to the conventional reaction (ICT to αKG), and thus we were surprised to find that the αKG molecule and catalytic residues were not primed for catalysis within the R132Q:NADPH:αKG:Ca^{2+} monomers. When superposing the quaternary ICT-bound and both αKG-bound R132Q monomers, the ICT molecule bound more equidistant between NADP(H) and the catalytic residue Y139, while αKG was found closer to NADP(H) (Fig 6E). HDX-MS analysis also showed differences when comparing ICT-bound versus αKG-bound R132Q, with all αKG-treated R132Q experiments showing lower deuterium uptake compared to all ICT-treated R132Q experiments (Figs 3, 4). Specifically, peptides encompassing α4, α5, β4 and hinge regions were more protected against deuterium uptake in R132Q:NADP(H):αKG:Ca^{2+} compared to R132Q:NADP(H):ICT:Ca^{2+} (Figs 3, EV4, EV5). In structures of αKG-bound IDH1 R132Q, the α4 helix and hinge in particular were shifted compared to the more closed quaternary structures of R132Q (ICT-bound), WT (ICT-bound), and R132H (αKG-bound) (Fig 6E).

Additional differences among ICT- and αKG-bound structures of IDH1 R132Q were observed at the dimer interface. As described previously, the α10 regulatory segment (residues 271-285) was fully unwound and unstable in R132Q:NADP(H), consistent with WT:NADP(H) and R132H:NADP(H) structures (Fig 5). Unsurprisingly, the α10 regulatory segment was a fully folded helix in both the ICT- and αKG-bound quaternary forms of R132Q, just like the quaternary ICT-bound WT and αKG-bound R132H complexes (Figs 6, 7). However, these structural snapshots mask the unique environments experienced by this regulatory segment depending on which substrate is bound to IDH1 R132Q. Our HDX-MS experiments showed that the IDH1 R132Q α10 helix and surrounding areas (including the α9 helix) were much more protected from proton exchange in both αKG and αKG + Ca^{2+} conditions than in the ICT and ICT + Ca^{2+} conditions (Figs 4C, 3A, EV5). Interestingly, uptake of deuterium in this region was similar for all ICT-treated R132Q and WT conditions, while all corresponding αKG-treated R132Q conditions had the lowest deuterium uptake overall (Figs 3, EV4, EV5). While ternary complexes of WT and R132H had similar levels of deuterium uptake in this region (Fig 4B), addition of Ca^{2+} resulted in protection in WT, while the corresponding quaternary form of R132H maintained high levels of deuterium uptake (Fig 4C). IDH1 R132Q, like WT, was sensitive to Ca^{2+} treatment (Fig 4C). In general, among all WT, R132Q, and R132H species, R132Q and WT had the lowest deuterium uptake, while R132H had the highest deuterium uptake. Thus, it appeared that increased protection of the α9 and α10 helices from deuterium uptake was associated with more efficient conventional (WT, R132Q) and neomorphic (R132Q) reaction catalysis (Table 1).

The unique ICT and αKG binding conformations in IDH1 R132Q also significantly affected the hydrogen bonding and salt bridging network that many aldo-keto reductase enzymes employ to create a “seatbelt” that envelopes the NADP(H) cofactor (reviewed in (Sanli *et al*, 2003)). Indeed, this seatbelt was observed in the WT:NADP(H):ICT:Ca^{2+} quaternary structure, with residue R314 in α11 helix shifted inward to make interactions with D253’ and Q256’ in α9 of the adjacent monomer and with a water molecule (Fig 8A). In contrast, the NADP(H)-only bound R132Q, R132H, and WT structures did not have R314 in the proper configuration to generate the seatbelt interactions (Fig 8). The absence of the seatbelt was not limited to binary structures; no seatbelt was observed in the ternary ICT-bound or, more surprisingly, the closed, quaternary αKG-bound R132H structures (Fig 8) (Yang *et al*, 2010; Rendina *et al*, 2013). As no αKG-bound IDH1 WT structure is available at this time, we compared a structure of a non-R132 mutant, IDH1 G97D, which does generate D2HG but exhibits a high degree of structural similarities with IDH1 WT (Rendina *et al*, 2013). The αKG-bound form of G97D did not show a seatbelt conformation, either (Fig 8). Thus, in general, this was a feature uniquely reserved for ICT-bound IDH1 WT.

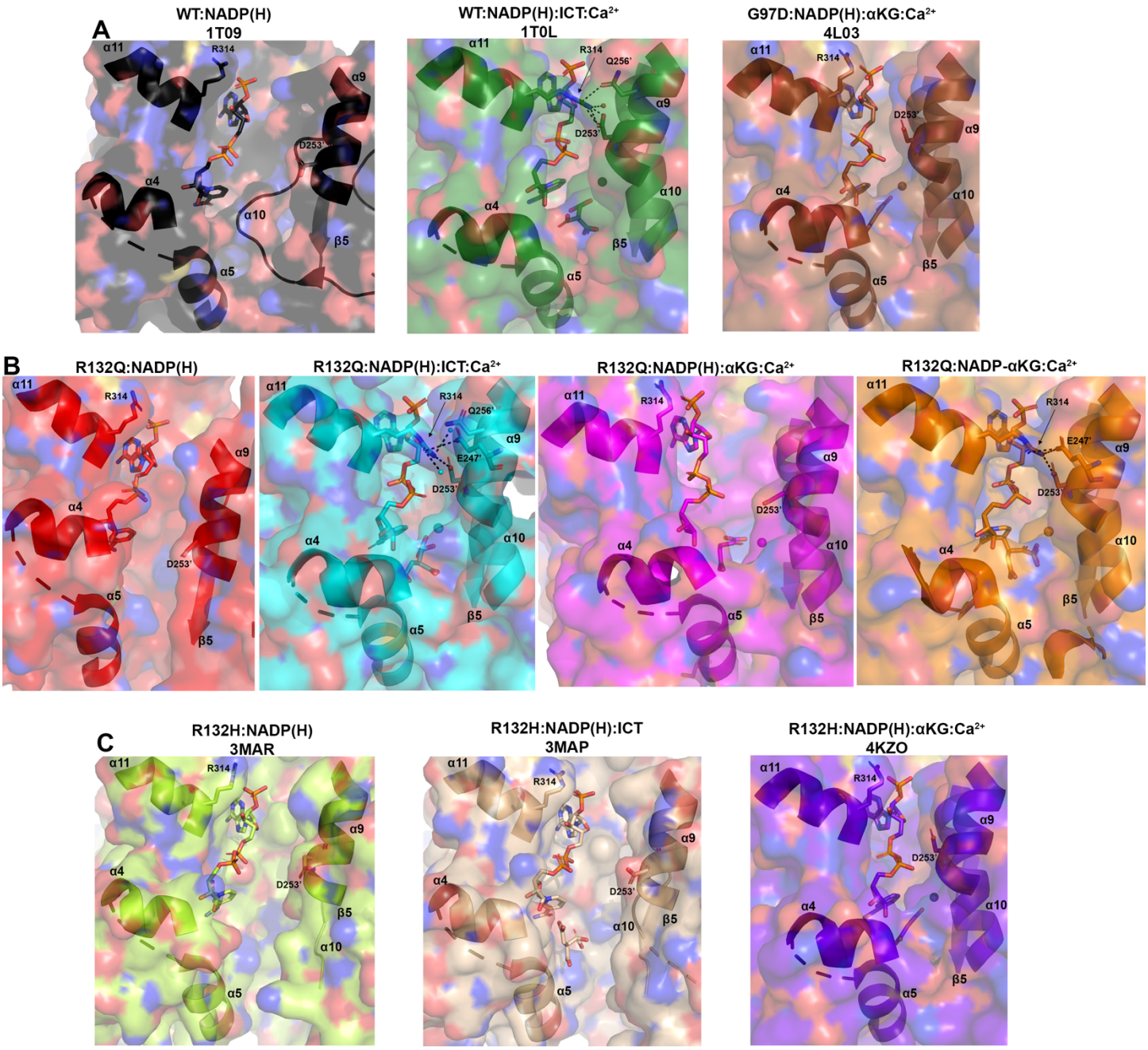

Figure 8. Hydrogen bond network facilitates a "seatbelt" that overlays NADP(H) in only some quaternary structures of IDH1. *A) The binary structure of IDH1 WT* (Xu *et al*, 2004) *and quaternary structure of G97D:NADP(H):αKG:Ca*$^{2+}$ (Rendina *et al*, 2013) *show a more open active site pocket with no seatbelt formation, while upon binding ICT and Ca*$^{2+}$*, residue R314 forms interactions with Q256', D253', and a water molecule to envelope the cofactor in the quaternary IDH1 WT complex* (Xu *et al*, 2004)*. B) While the binary R132Q:NADP(H) (red) and quaternary R132Q:NADP(H):αKG:Ca*$^{2+}$ *structures (magenta) show R314 is not in a suitable conformation to form a seatbelt over the cofactor, the R132Q:NADP(H):ICT:Ca*$^{2+}$ *structure (cyan) shows suitable interactions between R314 and Q256', D253', E247', and a water molecule. In the structure containing a NADP-αKG adduct in the most closed conformation (orange), a seatbelt is also formed via interactions of R314 only with E247' and D253'. C) The R314 residue is not in an appropriate conformation to form a seatbelt in any of the binary R132H:NADP(H), ternary R132H:NADP(H):ICT, or quaternary R132H:NADP(H):αKG:Ca*$^{2+}$ *structures of IDH1 R132H* (Rendina *et al*, 2013; Yang *et al*, 2010)*.*

When the seatbelt region was examined in the IDH1 R132Q structures, R132Q behaved like WT when binding the conventional reaction substrate (ICT), but more like R132H when binding the neomorphic substrate

(αKG). Specifically, like WT, the ICT-bound R132Q structure had residue R314 in position to contact Q256', D253', and, unique to this protein, E247' in β11 of the adjacent monomer, as well as a water molecule, to form a seatbelt over the cofactor (Fig 8B). Conversely, the αKG-bound R132Q structure in two of our three dimers had residue R314 swung away from the α9' helix, precluding the necessary polar contacts (one representative dimer shown in magenta, Fig 8B). Interestingly, the R132Q:NADP-αKG:Ca^{2+}/R132Q:NADP(H):Ca^{2+} dimer found in the closed conformation (Fig 7C) had an intact seatbelt over the NADP-αKG adduct (orange in Fig 8B). This provides an intriguing possibility that a fully closed conformation of αKG-bound IDH1 R132Q is possible if the nicotinamide ring of NADP(H) is stabilized in some way, including via a non-physiological adduct. Interestingly, HDX-MS dynamics showed that seatbelt formation was associated with an increase in deuterium uptake, with the α11 helix, which contains the seatbelt-forming R314 residue, more protected in the αKG-bound R132Q and R132H complexes relative to the ICT-bound WT and R132Q (seatbelt-forming) complexes (Fig 4).

IDH1 R132Q accommodates multiple NADP-containing adducts that may provide hints at transition-state-like features.

As described above, we report three unique dimers that all contain a NADP-αKG adduct (Fig 7G, Appendix Fig S1A) in one of their monomers. However, we also encountered an NADP-tris(2-carboxyethyl)phosphine (NADP-TCEP) adduct when attempting to crystallize ICT-bound to IDH1 R132Q (PDB ID 8VHE, Fig 7F, Appendix Fig S1B). To better understand how the NADP-TCEP and NADP-αKG adducts were forming, we first performed density functional theory (DFT) calculations for model NADP-TCEP and NADP-αKG adducts (Appendix Tables S1, S2), which suggested that adduct formation would fail to occur if not for the constraining environment of the crystal structure. The binding was energetically favored, and appeared to occur without barrier when vibrational effects were included, with a calculated binding energy of 9.4 kcal mol^{-1} at 298 K. However, the calculated free energies indicated that in solution, the entropy decrease would preclude spontaneous binding. Quenching the translational entropy of the species in the crystal may be what allowed the process to occur. We noted that the counterpoise corrections to the transition state and adduct energies were essential, having magnitudes of 7-8 kcal mol^{-1} and comparable to the uncorrected energy differences.

As these calculations suggested that binding of the NADP-TCEP adduct was a byproduct of crystallization, we considered an alternative possibility that the IDH1 R132Q active site itself favored adduct formation and binding. To explore this hypothesis, we first sought to determine if TCEP treatment affected IDH1 R132Q catalysis. If this adduct could form in the active site of IDH1 R132Q outside of the artificial environment of a crystal structure, TCEP would act as a competitive inhibitor as it essentially competes with both $NADP^+$ and ICT binding in adduct form. Further, we would observe inhibition in the conventional reaction only, as the neomorphic reaction requires NADPH. We thus challenged IDH1 R132Q catalysis with varying concentrations of three reducing agents: TCEP, dithiothreitol (DTT), and β-mercaptoethanol (BME). In general, it was only treatment with TCEP that resulted in dose-dependent inhibition of the ability of R132Q to catalyze the conventional reaction (Fig EV8, Appendix Table S3). More modest, though notable effects on catalysis

were also observed when challenging IDH1 WT with the highest concentration of TCEP tested (10 mM) (Fig EV9). Unsurprisingly, we did not observe any change in activity upon 10 mM TCEP treatment for the neomorphic reaction catalyzed by IDH1 R132H (k_{cat} = 1.0 ± 0.03, K_m = 0.42 ± 0.05) and by IDH1 R132Q (k_{cat} = 2.11 ± 0.07, K_m = 0.21 ± 0.04), which use NADPH as a substrate rather than $NADP^+$. These results strongly support the hypothesis that adduct formation occurs outside of the non-physiologically-relevant crystal packing environment.

The catalytic relevance of these adducts was also apparent when examining the active sites of the structures. In general, all adducts appeared as hybrids between the semi-closed αKG-bound R132Q complex and fully closed ICT-bound R132Q complex (Table 1). The NADP-αKG adduct-containing monomer in the most closed conformation (Fig 7C) aligned well to the fully closed ICT-bound R132Q monomer in all regions except the clasp domain, where the adducted monomer was shifted towards the dimer interface and the β9 strand was more intact (Fig 7G). This NADP-αKG adduct-containing monomer, as further evidence of its fully closed conformation, also showed the typical seatbelt feature with R314 of the α11 helix hydrogen bonding with residues in the β11 and α11 secondary structure (Fig 8B). In general, the TCEP and αKG carboxylates in the adduct helped coordinate the Ca^{2+} and maintained many hydrogen bonds in their respective active sites, though the metal ion was slightly shifted to accommodate the adduct (Figs 7G, 9). Together, this suite of monomers revealed that the adducts mimicked αKG binding, ICT binding, or transition between the two (Fig 9).

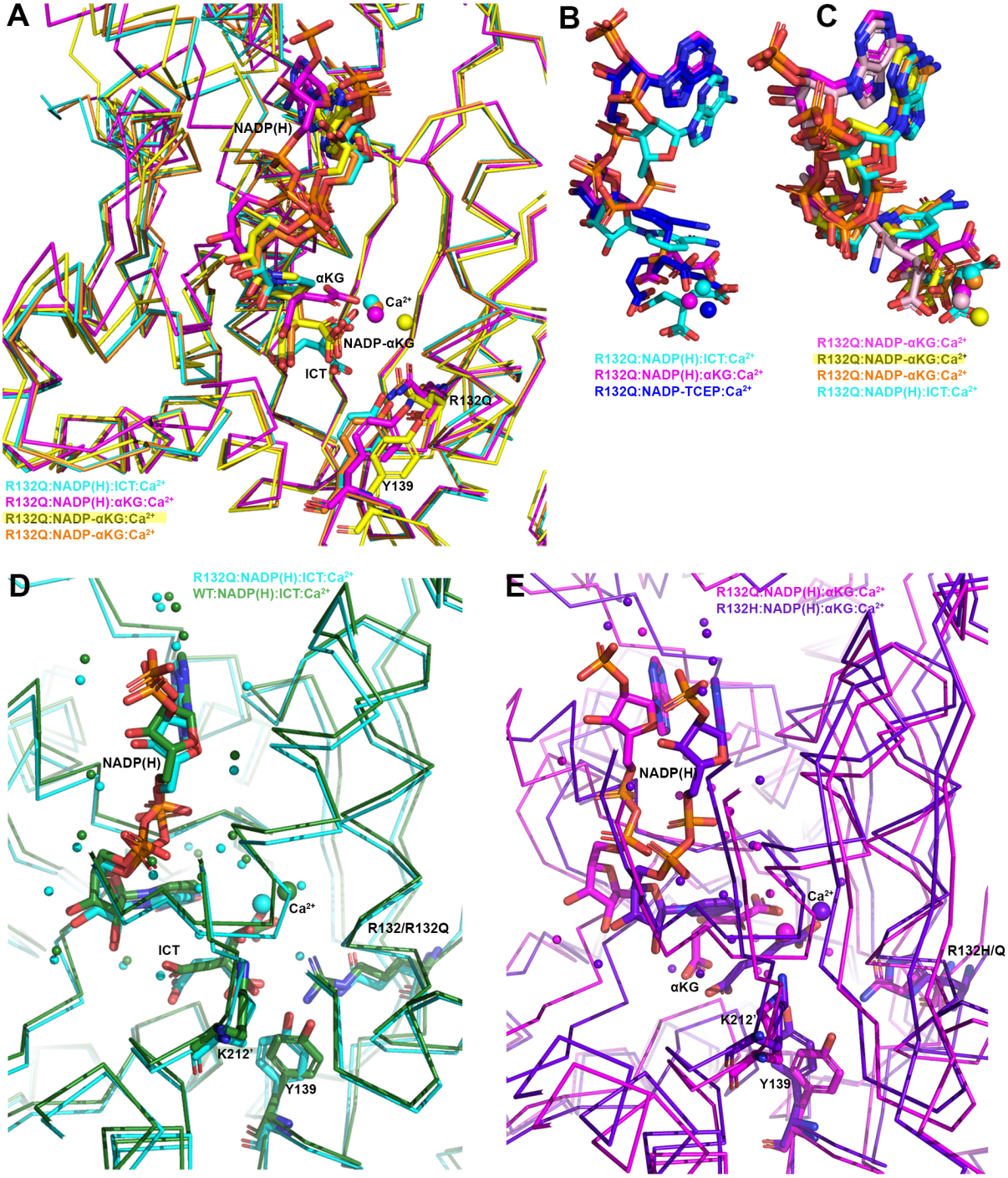

Figure 9. IDH1 R132Q structures have variation in substrate binding location, degree of nicotinamide ring puckering, and active site waters. *A) Monomer-based alignment of the more closed adduct-containing R132Q:NADP-αKG:Ca^{2+} monomer (orange) that aligns well with R132Q:NADP(H):ICT:Ca^{2+} (cyan), and a second adduct-containing R132Q:NADP-αKG:Ca^{2+} monomer (yellow) that aligns as a transition between the R132Q:NADP(H):ICT:Ca^{2+} (cyan) and R132Q:NADP(H):αKG:Ca^{2+} (magenta) monomers. Here the Ca^{2+} ion is likely not interacting with the NADP-αKG adduct and the catalytic residues are shifted. B, C) Only the NADP(H) and ICT or αKG, or the NADP-adduct, along with Ca^{2+}, are highlighted. Though the nicotinamide ring in the R132Q:NADPH:αKG:Ca^{2+} structure could not be modeled with confidence, comparisons of the planar nicotinamide ring of R132Q:NADP(H):ICT:Ca^{2+} versus the more puckered rings of the NADP-adducts are featured. Monomer-based alignment of R132Q:NADP(H):ICT:Ca^{2+} (cyan), R132Q:NADPH:αKG:Ca^{2+} (magenta), and R132Q:NADP-TCEP:Ca^{2+}(dark blue) are shown in B). Monomer-based alignment of R132Q:NADP(H):ICT:Ca^{2+} (cyan), R132Q:NADPH:αKG:Ca^{2+} (magenta), and the three observed*

R132Q:NADP-αKG:Ca^{2+} monomers (light pink, yellow, orange) are shown in C). D) Water molecules (smaller spheres) within 3.5 Å of the substrates are highlighted in ICT-containing structures. E) Water molecules (smaller spheres) within 3.5 Å of the substrates are highlighted in αKG-containing structures. Dimer-based alignments are shown in (D) and (E).

As these adducts showed hybrid binding features of αKG and ICT, we wondered if transition state features could be extrapolated from these structures. The structural features of the adduct's nicotinamide ring lent an interesting clue. Calculations on NAD(P) and NAD(P)H indicated that the oxidized form of the nicotinamide ring is predicted to be fully planar, while the reduced form is predicted to be in a boat conformation (Hammes-Schiffer, 2006; Meijers & Cedergren-Zeppezauer, 2009). Indeed, a survey of high resolution structures of proteins tended to have planar nicotinamide rings in the bound oxidized $NAD(P)^+$ molecules, though reduced forms were also generally reported as planar (Meijers & Cedergren-Zeppezauer, 2009; Plapp & Ramaswamy, 2012). During the course of turnover, the enzyme is predicted to distort the ring during the activation for hydride transfer, with the transition state posited to be highly puckered as a partial positive charge on C4N of the nicotinamide ring develops (Hammes-Schiffer, 2006; Meijers & Cedergren-Zeppezauer, 2009). Support for a puckered ring during the transition from oxidized to reduced cofactor has been described in a structure of horse liver alcohol dehydrogenase, where the puckered nicotinamide ring was in a quasi-boat conformation with bond angles and distances suggesting a strained molecule that could mimic a transition state (Plapp & Ramaswamy, 2012). Interestingly, NAD(P)-adducts with reducing agents have been reported previously, including with TCEP (Patel *et al*, 2020) and also with DTT (Paidimuddala *et al*, 2018), and were often found to have a more puckered nicotinamide ring.

Importantly, unlike the planar ring observed in our non-adducted forms of NADP(H) in the R132Q:NADP(H):ICT:Ca^{2+} complex, both the αKG- and TCEP-containing NADP adducts showed a more puckered nicotinamide ring (Fig 9, Appendix Fig S2, Appendix Table S2), suggestive of a transition-state-like conformation. Further, the carboxylic acid moieties of the TCEP and αKG portions of the adduct mimicked the locations of the carboxylic acid moieties of the bound ICT and αKG. Together, these findings suggest that the NADP-containing adducts may mimic transition state features of IDH1 R132Q turnover.

In summary, we highlight discrete catalytic and structural features among two tumor-relevant IDH1 mutants, with the IDH1 R132Q mutant serving as an invaluable tool to probe the journey through substrate turnover of two reactions that typically cannot be performed by the same enzyme. Together, our kinetics and static and dynamic structural data work suggests that substrate binding and conformational changes associated with the conventional and the neomorphic reactions have unique paths through turnover that can be described in terms of differences in substrate affinity, substrate binding site location, solvent accessibility, and propensity for conformational activation and active site remodeling. IDH1 R132Q's accommodation of catalytically-relevant adducts, perhaps due to its active site appearing better optimized for catalysis compared to R132H, illuminate snapshots of substrate analogs in varying degrees of catalytic readiness.

Discussion

The combination of steady-state and pre-steady-state kinetic experiments, HDX-MS, and X-ray crystallography reveals fundamental differences in the molecular mechanisms of catalysis by WT and IDH1 mutants. IDH1 R132Q, unlike R132H, was able to form a fully closed conformation with the seatbelt feature previously only seen in WT structures (Fig 8). In contrast, our suite of αKG-bound structures of R132Q featured an αKG binding site that was shifted slightly from that of ICT, with an overall semi-open conformation (Fig 8, 9). However, IDH1 R132Q was also able to fully close to a seatbelt-containing conformation upon the formation and binding of an unusual NADP-αKG adduct, which extended into the more typical ICT binding site (Fig 9C). While we do not expect this adduct to form under physiologically conditions, our experiments measuring inhibition by reducing agents were supportive of the possibility of these adducts representing catalytically meaningful conformations. Specifically, varying concentrations of ICT and TCEP with constant $NADP^+$ levels resulted in an unchanged k_{cat} for IDH1 R132Q (though kinetic parameters can become more error-prone when solubility and background absorbance issues preclude higher ICT concentrations) and decreasing K_m, indicating that the NADP-TCEP adduct was competitive with ICT. This was unsurprising as the TCEP portion of the adduct mimicked many features of ICT binding to IDH1 R132Q. While this experiment itself does not differentiate whether the adduct forms outside the protein and then binds, or whether the active site pocket itself drives adduct formation, our DTT experiments may help support a model where the enzyme supports adduct formation. As described, NADP-DTT adducts have been previously reported with yeast xylose reductase (Paidimuddala *et al*, 2018). While DTT has some similar structural features compared to ICT, it does not recapitulate the carboxylic acid features that TCEP and αKG provide in their NADP-containing adducts. Indeed, these carboxylic acid moieties in NADP-TCEP and NADP-αKG preserved many polar contacts that non-adducted NADP(H) and ICT form with Ca^{2+} and other active site features (Fig 9). Together, these data show that unlike R132H, IDH1 R132Q can sample a full range of a full range of open, semi-open and closed conformations upon binding both conventional and neomorphic reaction substrates (Fig 10).

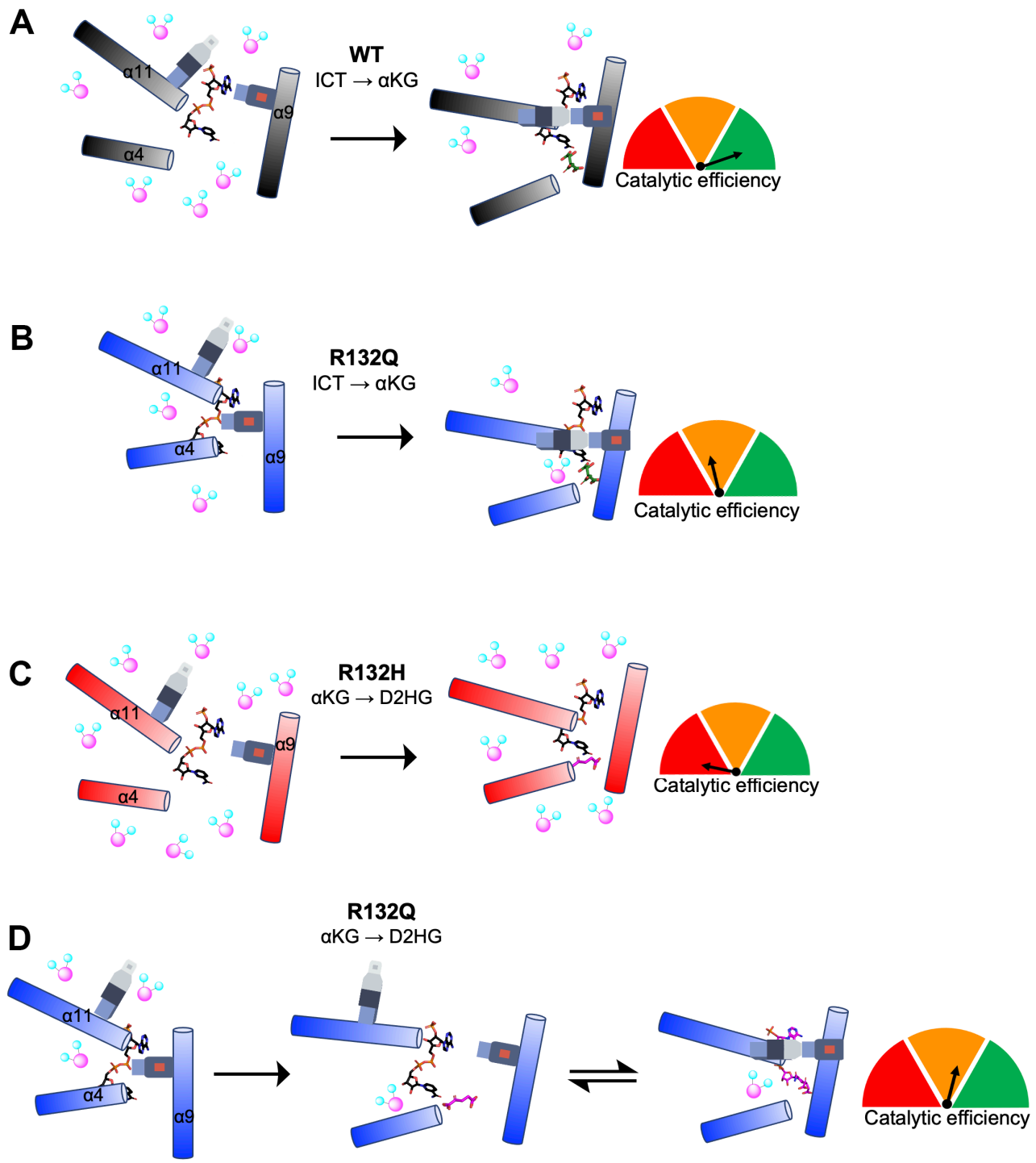

Figure 10. Conformations and solvent accessibility of IDH1 WT, R132Q, and R132H upon substrate binding. *Helices displaying unique movements upon dimer alignment in the three forms of IDH1 are highlighted. The seatbelt feature is indicated with a dark strip connecting the α11 and α9 helices. A) NADP(H)-only-bound IDH1 WT (Xu et al, 2004) collapses to a closed conformation upon ICT binding, though moderate levels of deuterium exchange are still permitted. B) NADP(H)-only-bound IDH1 R132Q also fully collapses to a closed conformation upon ICT binding, showing improved catalytic efficiency for the conventional reaction and lower deuterium uptake compared to R132H. However, catalytic activity is much lower compared to IDH1 WT. C) NADP(H)-only-bound IDH1 R132H (Yang et al, 2010), like ICT-bound IDH1 WT, collapses to a fully closed conformation upon αKG binding (Rendina et al, 2013), but a seatbelt is not formed and deuterium uptake remains high. D) NADP(H)-only-bound IDH1 R132Q forms semi-closed and closed conformations upon binding αKG and NADP-αKG, respectively, with a seatbelt successfully formed in the latter case. The αKG binding site was shifted away from the α9 helix, though activity was much higher than that seen in R132H.*

As ICT-bound R132Q better mimicked the fully closed, catalytically active conformation of ICT-bound WT in terms of active site and back cleft distances, location of catalytic residues and ICT binding site, and preservation of the seatbelt feature, we might have predicted that the conventional reaction would be catalytically more efficient. However, IDH1 R132Q drove the neomorphic reaction more efficiently than the conventional reaction. Rather than viewing the neomorphic reaction as the result of a failed conventional (reverse) reaction, as may be the case with IDH1 R132H, we instead posit that R132Q optimized the neomorphic reaction by employing structural features that facilitated enzyme activation. In addition to our finding that the binary R132Q complex is more solvent protected than binary R132H, we also found evidence of a more activated ground state by monitoring the degree of back cleft closing in the binary complex. As noted, an open back cleft is associated with a catalytically active conformation, while a closed back cleft is seen in the open, catalytically inactive forms (Xu *et al*, 2004). We employed two angle measurements that can monitor movement in the α3 and α6 helices relative to α12 (θ_1) and in the α6 and α12 helices (θ_2, Appendix Fig S4). Angles for R132Q:NADP(H) were notably higher than for R132H:NADP(H) (Yang *et al*, 2010), indicating a more open (i.e. more catalytically ready) back cleft. These angles were smaller in IDH1 R132Q in both ICT- and αKG-bound forms compared to the αKG-bound R132H (Rendina *et al*, 2013), indicating less movement was required to achieve the activated R132Q state for either reaction than to form the activated R132H state (Appendix Table S4). While these smaller back cleft angles were also associated with slightly larger active site pockets in the fully substrate-bound form of IDH1 R132Q, this region still maintained a highly solvent-protected environment (Figs 3, 4). Nonetheless, we sought to determine if these R132Q structures were associated with larger volumes in the active site using the software tool CAVER (Jurcik *et al*, 2018; Chovancova *et al*, 2012; Pavelka *et al*, 2016). While results were somewhat inconclusive, pockets identified in the ICT-bound R132Q and αKG-bound R132Q structures were quite unique, with the ICT-bound form showing much larger pockets more akin to the pockets present in ICT-bound WT and αKG-bound R132H (Xu *et al*, 2004; Rendina *et al*, 2013) (Appendix Fig S4). Thus, it appears that to preserve both normal and neomorphic activity, IDH1 R132Q does not simply recapitulate all features found in ICT-bound WT or in αKG-bound R132H, respectively. Instead, the improved activity that IDH1 R132Q has over R132H occurs via optimized structural adjustments that support more efficient catalysis.

While prominent differences in kinetic and structural features were observed when comparing R132Q with R132H, we also observed profound differences when comparing WT with mutant IDH1. It is unsurprising that IDH1 WT is far more efficient at catalyzing the conventional reaction than both R132Q and R132H since the arginine at residue 132 coordinates the C3 carboxylate of isocitrate (Pietrak *et al*, 2011), with R100 and R109 also participating in ICT coordination (Xu *et al*, 2004). As both mutants are no longer able to coordinate ICT's C3 carboxylate, it is not immediately obvious why the conventional reaction activity is much more efficient in R132Q versus R132H. One interesting clue was noted in the active sites of our crystal structures; the IDH1 R132Q mutant employed a unique active site water to mitigate the loss of hydrogen bonding to ICT resulting from the R to Q mutation. R100 and R109 in IDH1 R132Q were still properly oriented to help coordinate ICT, and these residues and Q132 plus the water provided hydrogen bonding interactions that imperfectly mimic the polar interactions with the substrate normally afforded by R132 in WT (Fig EV10A).

Notably, this water molecule was absent in the binary NADP(H)-bound forms of WT, R132Q, and R132H (Fig EV10C). We noticed a similar compensatory mechanism in our αKG-bound R132Q structure. Despite the local shifting of the αKG binding site in the R132Q active site, a water molecule that recapitulated the polar interactions normally made by residue R132 was again coordinated by R100, R109, and Q132, though the water molecule did not appear to hydrogen bond with the substrate (Fig EV10B). Instead, a second water molecule was found at the same location as the Ca^{2+} ion in the quaternary ICT-bound WT IDH1 structure (Fig EV10A), which presumably helped stabilize the αKG substrate in IDH1 R132Q. Notably, this water molecule was absent in the αKG-bound R132H structure (Fig EV10B). We have previously reported the importance of water molecules in facilitating mutant IDH1 inhibition (Chambers *et al*, 2020), and this current work highlights the importance of water in substrate binding by providing a possible mechanism by which R132Q is more catalytically efficient compared to R132H.

The inability of IDH1 R132H to employ a water molecule to properly coordinate ICT may also play a role in substrate binding in this mutant. In a previously solved structure of IDH1 R132H, ICT appears to bind in a slightly shifted location in the absence of Mg^{2+}/Ca^{2+} compared to WT (Yang *et al*, 2010). This was reported as a pre-binding site that stabilized a semi-closed conformation. It was posited that in IDH1 WT, ICT may also sample a pre-binding site in a semi-closed conformation before the enzyme rapidly closes into its more stable, catalytically competent conformation, though a structure capturing this state has not been reported (Yang *et al*, 2010). We have shown evidence of a pre-binding, semi-open conformation in IDH1 WT in previous HDX-MS experiments, but there we drove formation of this state by withholding the divalent metal (Sabo *et al*, 2023). It has been previously shown that a complex of Mg^{2+} and ICT is preferred by WT, while R132H binds Mg^{2+} and substrate (here, αKG) separately and with lower affinity for the metal ion (Liu *et al*, 2021). Importantly, it was proposed that WT's high affinity for metal ions led to a conformation that precluded mutant IDH1 inhibitor binding, suggesting one mechanism for inhibitor selectivity (Liu *et al*, 2021). Our data are supportive of these findings; we show that addition of Ca^{2+} led to minimal changes in deuterium uptake by substrate-bound R132H, while profound protection was seen upon addition of this metal ion to substrate-bound R132Q and WT (Fig EV4), suggesting metal ions facilitate and are required for the fully closed conformations in R132Q and WT, but not R132H.

Metal affinity is not the only selectivity filter for selective mutant IDH1 inhibitor binding; the dynamics of the α10 regulatory segment has been shown to significantly alter inhibitor binding (Xie *et al*, 2017). In structures of IDH1 R132H, this regulatory segment is a disordered loop in the open and semi-open conformations (Rendina *et al*, 2013; Yang *et al*, 2010), and helical only in the αKG-bound R132H structure. We have shown previously that IDH1 R132Q binds poorly to selective mutant IDH1 inhibitors, with IC_{50} profiles consistent with IDH1 WT rather than R132H (Avellaneda Matteo *et al*, 2018). We had predicted that a much more stable α10 regulatory segment in R132Q:NADP(H) drove this resistance. Here, we found that while this unfolded loop indeed had stronger electron density compared to R132H:NADP(H) (Yang *et al*, 2010), it still appeared less stable than the partially folded features of WT:NADP(H) (Xu *et al*, 2004). Instead, we now believe that the more activated, quaternary-like state of the binary R132Q:NADP(H) complex may play a larger role in inhibitor resistance. In the cofactor-only bound IDH1 R132Q complex, features such as the α11 and α4

helices were shifted inwards and the protein experienced less deuterium uptake (Fig 10). Using the allosteric inhibitor compound 24 as a prototypical selective mutant IDH1 inhibitor (6O2Y (Lin *et al*, 2019)), it appeared that the small increase in the stability of the α10 regulatory segment in IDH1 R132Q over R132H only slightly drove IDH1 R132Q's decreased mutant IDH1 inhibitor affinity (Fig EV11). Instead, our alignments showed that the region of the inhibitor binding pocket that included residues 111-121, which form a loop between the β4 and β5 strands, likely have a larger role in the loss of affinity towards inhibitors for IDH1 R132Q. While structural alignments show, unsurprisingly, that the inhibitor would be accommodated into this region in IDH1 R132H (Fig EV11E), these residues would interfere with inhibitor binding to R132Q (Fig EV11C). Importantly, residues 111-121 were shifted away in WT:NADP(H) similar to R132H:NADP(H), and thus this region in WT IDH1 appeared to accommodate this inhibitor quite well (Fig EV11D). Thus, while the α10 regulatory segment precludes inhibitor binding in IDH1 WT, it is instead residues 111-121 that prevent inhibitor binding in R132Q (Fig EV11A). This suggests that the essentially kinetically identical inhibitory characteristics of IDH1 WT and R132Q develop through two very different mechanisms. As this loop would not have been readily apparent as a selectivity gate when only examining the IDH1 WT structure, our R132Q:NADP(H) structure highlights possible novel resistance strategies.

While much effort has been devoted to understanding the unique catalytic and structural features of IDH1 WT versus R132H, our discovery of the unusual kinetic properties of the IDH1 R132Q mutant allowed a valuable opportunity to establish the static and dynamic structural adjustments required to maintain conventional and neomorphic activities within the same active site. Compared to IDH1 R132H, our findings show that the IDH1 R132Q binding pocket and surrounding areas are better primed for substrate binding and hydride transfer steps. Rather than simply acting as a hybrid of WT and R132H, IDH1 R132Q employed unique strategies to yield improved catalytic parameters for both ICT and αKG turnover as compared to R132H. These structural and dynamic discoveries not only highlight mechanistic properties of important tumor drivers, but also identify novel regions that may serve as selectivity handles when designing mutant IDH1 inhibitors requiring increasing selectivity or optimization against resistance mutants.

Materials and Methods

Reagent and tools. Dithiothreitol (DTT), isopropyl 1-thio-β-D-galactopyranoside (IPTG), Triton X-100, α-ketoglutaric acid sodium salt (αKG), DL-isocitric acid trisodium salt hydrate, and magnesium chloride ($MgCl_2$) were obtained from Fisher Scientific (Hampton, NH). BME was obtained from MP Biomedicals (Santa Ana, CA). β-Nicotinamide adenine dinucleotide phosphate reduced trisodium salt (NADPH), β-Nicotinamide adenine dinucleotide phosphate disodium salt ($NADP^+$) and tris(2-carboxyethyl)phosphine) (TCEP) was purchased from Millipore Sigma (Burlington, MA). Nickel-nitrilotriacetic acid (Ni-NTA) resin was obtained from Qiagen (Valencia, CA). Stain free gels (4-12%) were obtained from Bio-Rad Laboratories (Hercules, CA). Protease inhibitor tablets were obtained from Roche Applied Science (Penzberg, Germany). Phenylmethylsulfonyl fluoride (PMSF) salt was purchased from Thermo Scientific (Waltham, MA). The *Escherichia coli* BL21 Gold DE3 strain was used for all protein expression.

Purification of IDH1 WT and mutant. Human IDH1 WT, R132H, and R132Q homodimers were expressed from a pET-28b(+) plasmid and purified as described previously (Avellaneda Matteo *et al*, 2017) for steady-state kinetic analysis. For pre-steady-state kinetics and HDX-MS experiments, protein was loaded onto a pre-equilibrated (50 mM Tris-HCl 7.5 at 4 °C and 100 mM sodium chloride) Superdex 16/600 size exclusion column (GE Life Sciences, Chicago, IL) following Ni-NTA affinity chromatography to remove any protein aggregate. Protein was eluted with 50 mM Tris-HCl pH 7.5 at 4 ºC, 100 mM NaCl, and 1 mM DTT. The fractions were pooled and concentrated for use in pre-steady-state experiments, or pooled and dialyzed in Tris-HCl pH 7.5 at 4 ºC, 100 mM NaCl, 20% glycerol, and 1 mM DTT and used immediately for HDX-MS analysis (Sabo *et al*, 2023). For IDH1 R132Q X-ray crystallography experiments, two 1 L cultures of terrific broth supplemented with 50 µg/ml of kanamycin were incubated at 37 °C and 180 rpm until an A_{600} of 0.4 was reached. Cultures were removed and placed onto stir plates and allowed to cool to 25 °C. Expression was induced when cultures reached an A_{600} of 0.8-1.0 with 1 mM IPTG and incubated for an additional 16-18 hours. Cell pellets were harvested and resuspended in lysis buffer (20 mM Tris pH 7.5 at 4 °C, 500 mM NaCl, 0.2% Triton X-100, 5 mM imidazole, 1 mM PMSF, and 5 mM BME). Following cell lysis via sonication, crude lysate was clarified via centrifugation at 14,000 x *g* for one hour. The lysate was loaded on to a pre-equilibrated Ni-NTA column. The column was washed with 100 mL of wash buffer (20 mM Tris pH 7.5 at 4 °C, 500 mM NaCl, 15 mM imidazole, 5 mM BME). Protein was eluted using elution buffer (50 mM Tris pH 7.5 at 4°C, 500 mM NaCl, 500 mM imidazole, 5% glycerol, 10 mM BME). For the NADP(H)-stripped experiments, a buffer containing αKG was passed through the Ni-NTA affinity column prior to elution as described in previous work (Rendina *et al*, 2013). In all cases, eluted protein was loaded onto a HiPrep 26/10 desalting column (GE Healthcare) containing 25 mM Tris pH 7.5 at 20 °C, 500 mM NaCl, 5 mM EDTA, 2 mM DTT, and placed on ice overnight to remove any remaining metals from purification. Fractions containing IDH1 were concentrated (MilliPore Amicon Ultra 15 30 kDa NMWL concentrator) and loaded onto a Superdex 26/600 (GE Healthcare) pre-equilibrated with 20 mM Tris pH 7.5 at 20 °C, 200 mM NaCl, and 2 mM DTT. Fractions containing pure IDH1 were pooled and concentrated to a final concentration of 14-20 mg/mL, flash frozen using liquid nitrogen, and stored at -80 °C. In all cases, the purity of the protein (>95% was confirmed using SDS-PAGE analysis).

Molecular graphics images. Structure figures were prepared using PyMOL(Schrödinger, LLC. The PyMOL Molecular Graphics System, Version 2.5.2). Pocket volumes were calculated using CAVER Analyst 2.0 BETA (Jurcik *et al*, 2018; Chovancova *et al*, 2012; Pavelka *et al*, 2016). Cavity computations used a 1.4 Å probe and 3.0 Å max probe including all pockets in all computations. Pocket volume precision was increased and samples were taken from a minimum of 5100 samples.

Kinetics assays. To measure steady-state activity of homodimer WT, R132H, and R132Q, only minor modifications were made from previous studies (Avellaneda Matteo *et al*, 2017, 2018). For the conventional reaction (ICT to αKG), IDH1 buffer (50 mM Tris HCl pH 7.5 at 37 °C, 150 mM NaCl, 10 mM $MgCl_2$, 1 mM DTT) and homodimer IDH1 (100 nM IDH1 WT, or 200 nM IDH1 R132H and R132Q), as well as various concentrations of ICT and 200 µM $NADP^+$ were preincubated separately for 3 min at 37 °C. Following addition of substrates at 37 °C, the increase of absorbance at 340 nm due to production of NADPH was monitored using an Agilent Cary UV/Vis 3500 spectrophotometer (Santa Clara, CA). For the neomorphic reaction (αKG to

D2HG), IDH1 buffer and homodimer mutant IDH1 (200 nM) as well as various concentrations of αKG at pH 7.5 and 200 μM NADPH were separately preincubated for 3 min at 37 °C. Following addition of substrates at 37 °C, the decrease of absorbance at 340 nm due to consumption of NADPH was monitored. The kinetic parameters, which were obtained using at least two unique protein preparations, were determined as described previously (Avellaneda Matteo *et al*, 2017, 2018).

For the reducing agent inhibition steady-state studies, the conventional reaction conditions described above were repeated except one of three reducing agents (DTT, TCEP, or BME) were added at varying concentrations during the pre-incubation step with the enzyme before substrates were added. Upon obtaining Michaelis-Menten plots at various reducing agent concentrations, the inverse of both k_{obs} and substrate concentration were plotted in Lineweaver-Burk analysis.

Single-turnover pre-steady-state kinetic assays were performed for the neomorphic reaction at 37 ºC using an RSM stopped-flow spectrophotometer (OLIS, Atlanta, GA). For the neomorphic reaction, depletion of NADPH signal as a function of time was monitored by exciting the sample at 340 nm and scanning the emission spectrum from 410 to 460 nm. Final concentrations after mixing were as follows: 40 μM IDH1 R132Q or R132H, 10 μM NADPH, 10 mM αKG (IDH1 R132H) or 0.5 mM αKG (IDH1 R132Q), 50 mM Tris-HCl (pH 7.5 at 37 ºC), 150 mM NaCl, 0.1 mM DTT, and 10 mM $MgCl_2$. The change in fluorescence as a function of time was fit to a single exponential equation ($Y = A_0e^{-kt}$) using Graphpad Prism to obtain k_{obs}. For IDH1 R132H, a higher concentration of αKG (20 mM) was used since 1 mM αKG showed an initial lag.

Single turnover pre-steady-state kinetics were also performed for the conventional reaction at 37 ºC to obtain rate constants associated with steps after $NADP^+$ binding through hydride transfer using an RSM stopped-flow spectrophotometer. NADPH formation as a function of time was similarly monitored by exciting at 340 nm and scanning the emission spectrum from 410 to 460 nm. Final concentrations after mixing were as follows: 30 μM IDH1 WT or R132Q, 10 μM $NADP^+$, 0.5 mM ICT (IDH1 WT) or 1 mM ICT (IDH1 R132Q), 50 mM Tris-HCl (pH 7.5 at 37 ºC), 150 mM NaCl, 0.1 mM DTT, and 10 mM $MgCl_2$. The change in fluorescence as a function of time was fit to a single exponential equation ($Y = A_0e^{-kt}$) using Graphpad Prism and k_{obs} values were obtained.

Rates associated with NADPH binding corresponding to the first step of the catalytic cycle for the neomorphic reaction were performed as previously described (Rendina *et al*, 2013) using an RSM-stopped flow spectrophotometer (OLIS, Atlanta, Georgia). However, due to low sensitivity of our stopped-flow spectrophotometer, the concentrations of NADPH and IDH1 were increased 10-fold, which in the case of IDH1 WT led to rates too fast to be detected by our instrument (≤100 s^{-1}). Therefore, glycerol (40%) and temperature (10 ºC) were used to slow NADPH binding rates to IDH1. NADPH binding as a function of time was monitored by exciting at 340 nm and scanning the emission spectrum from 410 to 460 nm. Final concentrations after mixing were as follows: 4 μM IDH1, varying concentration of μM $NADP^+$, 100 mM Tris-HCl pH 7.5, 150 mM NaCl, 0.1 mM DTT, 10 mM $MgCl_2$, and 40% glycerol. The change in fluorescence as a function of time was fit to a single exponential equation ($Y = A_0e^{-kt}$) using Graphpad Prism, and k_{obs} values were obtained and plotted as a function of NADPH concentration using the equation $k_{obs} = k_1[NADPH] + k_{-1}$. This yielded a linear graph indicating one-step binding, with the slope equal to k_1 and the Y-intercept equal to k_{-1}.

Isothermal titration calorimetry (ITC) experiments were conducted at the Sanford Burnham Prebys Protein Production and Analysis Facility using a Low Volume Affinity ITC calorimeter (TA Instruments). For NADPH titrations, experiments were performed at 25 ºC in 20 mM Tris pH 7.5, 100 mM NaCl, 10 mM $MgCl_2$, and 2 mM BME, injecting 0.25 mM NADPH into the cell containing 0.025 mM for IDH1 WT, 0.025 mM or 0.04 mM IDH1 R132H; and injecting 0.15 mM NADPH into the cell containing 0.034 mM or 0.026 mM IDH1 R132Q. For ICT titrations, experiments were performed at 25 ºC in 20 mM Tris pH 7.5, 100 mM NaCl, 10 mM $CaCl_2$, and 2 mM BME, injecting 0.6mM ICT into the cell containing 0.12 mM IDH1 R132Q or 0.13 mM IDH1 R132H. Baseline control experiments were performed by injecting the ligand into a cell with buffer only. In all cases, ITC data were analyzed using the Nanoanalyze software package by TA Instruments.

HDX-MS data collection and analysis. HDX-MS data collection and analysis was performed at the Biomolecular and Proteomics Mass Spectrometry Facility (BPMSF) of the University California San Diego using a Waters Synapt G2Si system with HDX technology (Waters Corporation, Milford, MA) as previously described, again using a sample of IDH1 WT without substrates to be analyzed alongside every experiment to allow experiment to experiment comparisons (Sabo *et al*, 2023; Peacock *et al*, 2018). Deuterium exchange reactions were conducted using a Leap HDX PAL autosampler (Leap Technologies, Carrboro, NC). The D_2O buffer was prepared by lyophilizing dialysis buffer (50 mM Tris buffer at pH 7.5 at 4 ºC, 100 mM NaCl, and 1 mM DTT) either alone (IDH1:NADP(H) condition) or with the following ligands: for the conventional reaction experiments, IDH1 WT and R132Q were treated with 0.01 mM $NADP^+$ and 10 mM ICT (ternary complexes), or with 0.1 mM $NADP^+$, 10 mM ICT, and 10 mM $CaCl_2$. For the neomorphic reaction experiments, IDH1 R132Q and R132H were treated with 0.1 mM NADPH and 10 mM αKG (ternary complexes), or with 0.1 mM NADPH, 10 mM αKG, and 10 mM $CaCl_2$ was also included (quaternary complexes). The buffer was first prepared in ultrapure water and then redissolved in an equivalent volume of 99.96% D_2O (Cambridge Isotope Laboratories, Inc., Andover, MA) just prior to use. Deuterium exchange measurements were performed in triplicate for every time point (in the order of 0 min, 0.5 min, 1 min, 2 min, 5 min); each run took 30 min to complete. Samples were prepared ~ 30 min prior to experimental setup and stored at 1 ºC until dispensing into reaction vials at the start of the reaction, resulting in samples that were exposed to its deuterium buffer between 2 h (0.5 min timepoint) and 7.5 h (last replicate of the 5 min timepoint) at 1 ºC. Protein (4 µL) alone or with ligands were equilibrated for 5 min at the reaction temperature (25 ºC) before mixing with D_2O buffer (56 µL, +/- ligands depending on condition). A solution of 3 M guanidine hydrochloride (50 µL, final pH 2.66) was added to each sample (50 µL) with incubation for 1 min at 1 ºC to quench deuterium exchange. The quenched sample (90 µL) was injected into a 100 uL sample loop for in-line digestion at 15 ºC using pepsin column (Immobilized Pepsin, Pierce). Peptides were then captured on a BEH C18 Vanguard precolumn and then separated by analytical chromatography (Acquity UPLC BEH C18, 1.7 µm 1.0 × 50 mm, Waters Corporation) over 7.5 min using a 7-85% acetonitrile gradient containing 0.1% formic acid. Samples were then electrosprayed into a Waters Synapt G2Si quadrupole time-of-flight mass spectrometer. Data were collected in the Mobility, ESI+ mode (mass acquisition range = 200–2000 (m/z); scan time = 0.4 s). An infusion of leu-enkephalin (m/z = 556.277) every 30 s (mass accuracy of 1 ppm for calibration standard) was used for continuous lock mass correction.

To identify peptides, data was collected on the mass spectrometer in mobility-enhanced data-independent acquisition (MS^E), mobility ESI+ mode. Peptide masses were determined from triplicate analyses, and resulting data were analyzed using the ProteinLynx global server (PLGS) version 3.0 (Waters Corporation). We identified peptide masses using a minimum number of 250 ion counts for low energy peptides and 50 ion counts for their fragment ions, with the requirement that peptides had to be larger than 1,500 Da in all cases. Peptide sequence matches were filtered using the following cutoffs: minimum products per amino acid of 0.2, minimum score of 7, maximum MH+ error of 5 ppm, and a retention time RSD of 5%. To ensure high quality, we required that all peptides were present in two of the three experiments. After identifying peptides in PLGS, we then used DynamX 3.0 data analysis software (Waters Corporation) for peptide analysis. Here, relative deuterium uptake for every peptide was calculated via comparison of the centroids of the mass envelopes of the deuterated samples with non-deuterated controls per previously reported methods (Wales *et al*, 2008), and used to obtain data for coverage maps. Data are represented as mean values +/- SD of the three technical replicates due to processing software limitations, but we note that the LEAP robot provides highly reproducible data for biological replicates. Back-exchange was corrected for in the deuterium uptake values using a global back exchange correction factor (typically ~25%) determined from the average percent exchange measured in disordered termini of varied proteins (Ramsey *et al*, 2017). Significance among differences in HDX data points was assessed using ANOVA analyses and t tests (*p* value cutoff of 0.05) within DECA (Lumpkin & Komives, 2019). We generated deuterium uptake plots in DECA (github.com/komiveslab/DECA), with data plotted as deuterium uptake (corrected) versus time. An HDX-MS data summary table is shown in the Appendix Table S5, and percent uptake plots are shown in the Source Data files. *HDX-MS data will be uploaded to a MASSIVE repository with accession number prior to manuscript publication.*

Crystallization. For the NADP(H)-only bound IDH1 R132Q crystals (PDB 8VHC, 8VH9), enzyme (14-20 mg/mL) was incubated on ice with 10 mM NADPH. Crystals of R132Q:NADP(H) were grown via hanging drop vapor diffusion at 4 °C. 2 µL of IDH1 were mixed with 2 µL of well solution containing either 220 mM ammonium sulfate, 100 mM bis-tris pH 6.5, and 20% (w/v) PEG 3350 (PDB ID 8VHC), or well solution containing 200 mM ammonium citrate tribasic pH 7.0 and 26% (w/v) PEG 3350 (8VH9).

IDH1 R132Q crystals containing ICT (8VHD) were grown by first incubating the enzyme at 20 mg/mL with 10 mM $NADP^+$, 10 mM $CaCl_2$, and 200 mM DL-isocitric acid at 20°C for 1 h. Then, 2 µL of IDH1 were mixed with 2 µL of well solution containing 100 mM bis-tris propane pH 6.5, 200 mM NaI, and 24% (w/v) PEG 3350 and stored at 4 °C. Crystals were harvested using a nylon-loop and cryo-protected using a solution of 100 mM bis-tris propane pH 6.5, 200 mM NaI, 26%(w/v) PEG 3350, and 20%(v/v) glycerol. Crystals were flash-frozen in liquid nitrogen and stored until data collection.

IDH1 R132Q crystals containing αKG and/or αKG-adducts were generated by incubating enzyme (14-20 mg/mL) on ice with 10 mM NADPH, 20 mM $CaCl_2$, 75 mM αKG Fisher Scientific (Hampton, NH) for 1 h. For the 8VHB structure, crystals were grown at 4°C via hanging drop vapor diffusion, where 2 µL of IDH1 were mixed with 2 µL of the well solution containing 200 mM NaSCN and 21%(w/v) PEG 3350. Crystals were cryo-protected using a solution of 20% (v/v) glycerol, 25% (w/v) PEG 3350 and 200 mM NaSCN, and flash-frozen in

liquid nitrogen and stored until data collection. For the 8VHA structure, IDH1 R132Q was incubated at 20 °C with 10 mM NADPH, 10 mM $CaCl_2$, 10 mM αKG, and then crystals were grown at 4 °C by mixing 2 µL of IDH1 R132Q with 2 µL of well solution containing 160 mM $NaNO_3$ and 20% (w/v) PEG 3350. Crystals were harvested using a nylon-loop and cryo-protected in a solution containing 22% (v/v) glycerol and 26% (w/v) PEG 3350.

For IDH1 R132Q crystals containing the NADP-TCEP adduct (8VHE), enzyme (14-20 mg/mL) was incubated on ice with 10 mM $NADP^+$, 20mM $CaCl_2$, and 75 mM DL-isocitric acid for 1 h. Crystals were grown at 4 °C via hanging drop vapor diffusion, with 1.5 µL of IDH1 mixed with 1.5 µl of well solution containing 200 mM KSCN, 24% (w/v) PEG 6000, and 5 mM TCEP pH 7.4.

Data collection, processing, and refinement. Data were collected at 100K using synchrotron radiation at the Advanced Photon Source, beamline 24-ID-E or at the Stanford Synchrotron Radiation Lightsource, beamline BL12-2. All datasets were processed with XDS (Kabsch, 2010). Structure solutions were obtained by molecular replacement using PHASER-MR in Phenix (Liebschner *et al*, 2019; Adams *et al*, 2010). For αKG and/or αKG-adducts (8VHB and 8VHA), isocitrate (8VHD), and NADP-TCEP (8VHE) co-crystals, PDB ensembles of 1T0L (Xu *et al*, 2004), 4KZO (Rendina *et al*, 2013), and 6PAY (Roman *et al*, 2019) were used for molecular replacement by generating ensembles using Phenix Ensembler (Liebschner *et al*, 2019; Adams *et al*, 2010). For IDH1 R132Q apo structures, 1T09 and 4UMX were used as search models. The models were optimized via iterative rounds of refinement in Phenix Refine and manual rebuilding in Coot (Emsley *et al*, 2010; Emsley & Cowtan, 2004). Ligand restraints were generated in Phenix eLBOW (Liebschner *et al*, 2019; Adams *et al*, 2010). Data collection and refinement statistics are summarized in Appendix Table S6.

Calculations. DFT calculations (Hohenberg & Kohn, 1964) were carried out to model the NADP-TCEP binding energetics and geometry using the Gaussian 16 suite of programs (Frisch *et al*, 2016). The $NADP^+$ was modeled as the nicotinamide ring plus a pendant dihydroxy furan to represent the sugar. The model $NADP^+$ and NADP-TCEP adduct were each given a +1 charge. To better model the effects of the solvent, three explicit water molecules were included in calculations on the adducts, distributed at the likeliest sites for hydrogen bonding. The B3LYP (Becke, 1993), ωB97XD (Chai & Head-Gordon, 2008), and M06 (Zhao & Truhlar, 2008) hybrid functionals were used with the cc-pVDZ (Dunning, 1989; Wilson *et al*, 1996) and pc-*n* (Jensen, 2001; Jensen & Helgaker, 2004) basis sets, with the latter obtained from the online Basis Set Exchange (Pritchard *et al*, 2019). In all of these calculations, implicit solvation was applied using the COSMO model with water as the solvent (Barone & Cossi, 1998; Cossi *et al*, 2003) and empirical dispersion was added using the D3 version of Grimme's dispersion along with Becke-Johnson damping (Grimme *et al*, 2010, 2011). This treatment of solvation effectively models the species as though they were in solution rather than crystalline form. Harmonic frequency analysis was carried out to obtain the vibrational corrections needed to calculate the free energies. Finally, because basis set superposition error can be substantial relative to intermolecular bond energies, the counterpoise correction was applied to our final energies of reaction (Boys & Bernardi, 1970; Simon *et al*, 1996). The transition state (TS) for the TCEP + NADP binding was identified and confirmed by analysis of the single imaginary vibrational frequency.

For the dihedral angles, the deviation from planarity $\Delta\theta$ of the NADP pyridine ring in the adduct was reported using the average of two dihedral angles. Numbering the carbon atoms in the ring by convention as shown in Appendix Fig S2, the C-P bond in NADP-TCEP formed at atom 4. The positions of the N atom 1 and the opposite C atom 4 are referenced to the plane defined by the roughly coplanar atoms 2, 3, 5, and 6. The average of the dihedral angles 2-3-5-4 and 6-3-5-4 (Appendix Fig S2) was subtracted from 180° to yield $\Delta\theta_{\mathrm{C}}$ as a metric for the deviation from planarity of C4, while the average of 3-2-6-1 and 5-2-6-1 subtracted from 180° is used to calculate $\Delta\theta_{\mathrm{N}}$ for N1. A sign convention was applied such that if $\Delta\theta_{\mathrm{C}}$ and $\Delta\theta_{\mathrm{N}}$ had the same sign, the two corners of the ring bend away each other in chair fashion, whereas opposite signs indicate a boat-like conformation. Comparison of the results from the different functionals and basis sets showed very little difference in the geometry. Optimized geometries obtained with the pc-2 basis set on a smaller geometry (omitting sugar and explicit waters) were not significantly different from those obtained with pc-1, so we chose to report the B3LYP/pc-1 results here, with the sugar and explicit waters included (Appendix Table S1). An additional geometry optimization was run on the NADP-αKG adduct with two explicit waters and a -2 charge, employing the aug-pc-1 basis set (Jensen, 2001, 2002) to obtain the diffuse functions necessary to adequately model anions.

Data Availability

Crystallographic data have been submitted to the PDB public repository. Output files from the computational work are available at the ioChem-BD database (https://doi.org/10.19061/iochem-bd-6-320). All remaining data generated or analyzed in this study are included in the manuscript and the Source Data files.

Acknowledgements

This work was funded by a Research Scholar Grant, RSG-19-075-01-TBE, from the American Cancer Society (C.D.S.), National Institutes of Health R35 GM137773 (C.D.S.), MARC 1 T34 GM149430 (C.D.S.), and IMSD 5R25GM058906 (SDSU), as well as the California Metabolic Research Foundation (SDSU) and the Rees-Steely Research Foundation (E.A.). The HDX-MS core of the UCSD BPMSF is supported by NIH shared instrumentation grant S10 OD0016234. The Sanford Burnham Prebys Protein Production and Analysis Facility is supported by NCI Cancer Center Support Grant P30 CA030199. The Northeastern Collaborative Access Team beamlines are funded by NIH/NIGMS (P30GM124165) and the Eiger 16M detector at the 24-ID-E beam line is funded by a NIH-ORIP HEI grant (S10OD021527). The Advanced Photon Source is a U.S. Department of Energy (DOE) Office of Science User Facility operated for the DOE Office of Science by Argonne National Laboratory under Contract No. DE-AC02-06CH11357. Use of the Stanford Synchrotron Radiation Lightsource, SLAC National Accelerator Laboratory, is supported by the U.S. DOE Office of Science, Office of Basic Energy Sciences under Contract No. DE-AC02-76SF00515. The SSRL Structural Molecular Biology Program is supported by the DOE Office of Biological and Environmental Research, and by NIH/NIGMS (P30GM133894). The content is solely the responsibility of the authors and does not necessarily represent the official views of the National Institutes of Health.

Author contributions

Matthew Mealka: investigation, data curation, software, formal analysis, validation, methodology, writing – review and editing; Nicole Sierra: investigation, data curation, software, formal analysis, visualization, methodology, writing – review and editing; Diego Avellaneda Matteo: investigation, data curation, software, formal analysis, validation, methodology, visualization writing – review and editing; Elene Albekioni: investigation, data curation, software, formal analysis, validation, methodology, visualization, writing – review and editing; Rachel Khoury: investigation, data curation, software, formal analysis, visualization, methodology, writing – review and editing; Timothy Mai: investigation, software, formal analysis, validation, visualization, writing – review and editing; Brittany Conley: investigation, software, formal analysis, validation, visualization, writing – review and editing; Nalani J. Coleman: investigation, data curation, software, formal analysis, visualization, methodology, writing – review and editing; Kaitlyn A. Sabo: investigation, data curation, software, formal analysis, visualization, methodology, writing – review and editing; Elizabeth A. Komives: funding acquisition, writing – review and editing; Andrey A. Bobkov: data curation, software, formal analysis, validation, methodology, writing – review and editing; Andrew L. Cooksy: investigation, data curation, software, formal analysis, validation, visualization, methodology, writing – review and editing; Steve Silletti: data curation, methodology, formal analysis, validation, writing – review and editing; Jamie Schiffer: investigation, data curation, visualization, software, formal analysis, methodology, writing – review and editing; Tom Huxford: conceptualization, formal analysis, supervision, visualization, writing – review and editing; Christal D. Sohl: conceptualization, formal analysis, data curation, supervision, visualization, funding acquisition, writing – original draft, project administration, writing – review and editing.

Disclosure and competing interests statement

The authors declare that they have no conflicts of interest.

References

Adams PD, Afonine PV, Bunkoczi G, Chen VB, Davis IW, Echols N, Headd JJ, Hung LW, Kapral GJ, Grosse-Kunstleve RW, *et al* (2010) PHENIX: a comprehensive Python-based system for macromolecular structure solution. *Acta Crystallogr D Biol Crystallogr* 66: 213–21

Adeva J (2022) Current development and future perspective of IDH1 inhibitors in cholangiocarcinoma. *Liver Canc Intl* 3: 17–31

Avellaneda Matteo D, Grunseth AJ, Gonzalez ER, Anselmo SL, Kennedy MA, Moman P, Scott DA, Hoang A & Sohl CD (2017) Molecular mechanisms of isocitrate dehydrogenase 1 (IDH1) mutations identified in tumors: The role of size and hydrophobicity at residue 132 on catalytic efficiency. *J Biol Chem* 292: 7971–7983

Avellaneda Matteo D, Wells GA, Luna LA, Grunseth AJ, Zagnitko O, Scott DA, Hoang A, Luthra A, Swairjo MA, Schiffer JM, *et al* (2018) Inhibitor potency varies widely among tumor-relevant human isocitrate dehydrogenase 1 mutants. *Biochem J* 475: 3221–3238

Balss J, Meyer J, Mueller W, Korshunov A, Hartmann C & von Deimling A (2008) Analysis of the IDH1 codon 132 mutation in brain tumors. *Acta Neuropathol* 116: 597–602

Barone V & Cossi M (1998) Quantum calculation of molecular energies and energy gradients in solution by a conductor solvent model. *J Phys Chem A* 102: 1995–2001

Becke AD (1993) Density-functional thermochemistry. III. The role of exact exchange. *J Chem Phys* 98: 5648–5652

Bleeker FE, Lamba S, Leenstra S, Troost D, Hulsebos T, Vandertop WP, Frattini M, Molinari F, Knowles M, Cerrato A, *et al* (2009) IDH1 mutations at residue p.R132 (IDH1(R132)) occur frequently in high-grade gliomas but not in other solid tumors. *Hum Mutat* 30: 7–11

Borger DR, Tanabe KK, Fan KC, Lopez HU, Fantin VR, Straley KS, Schenkein DP, Hezel AF, Ancukiewicz M, Liebman HM, *et al* (2012) Frequent mutation of isocitrate dehydrogenase (IDH)1 and IDH2 in cholangiocarcinoma identified through broad-based tumor genotyping. *Oncologist* 17: 72–9

Boys SF & Bernardi F (1970) The calculation of small molecular interactions by the differences of separate total energies. Some procedures with reduced errors. *Mol Phys* 19: 553–566

Casadevall G, Duran C & Osuna S (2023) AlphaFold2 and Deep Learning for Elucidating Enzyme Conformational Flexibility and Its Application for Design. *JACS Au* 3: 1554–1562

Cerami E, Gao J, Dogrusoz U, Gross BE, Sumer SO, Aksoy BA, Jacobsen A, Byrne CJ, Heuer ML, Larsson E, *et al* (2012) The cBio cancer genomics portal: an open platform for exploring multidimensional cancer genomics data. *Cancer Discov* 2: 401–4

Chai J-D & Head-Gordon M (2008) Long-range corrected hybrid density functionals with damped atom–atom dispersion corrections. *Phys Chem Chem Phys* 10: 6615–6620

Chambers JM, Miller W, Quichocho G, Upadhye V, Matteo DA, Bobkov AA, Sohl CD & Schiffer JM (2020) Water networks and correlated motions in mutant isocitrate dehydrogenase 1 (IDH1) are critical for allosteric inhibitor binding and activity. *Biochemistry* 59: 479–490

Chovancova E, Pavelka A, Benes P, Strnad O, Brezovsky J, Kozlikova B, Gora A, Sustr V, Klvana M, Medek P, *et al* (2012) CAVER 3.0: a tool for the analysis of transport pathways in dynamic protein structures. *PLoS Comput Biol* 8: e1002708

Chowdhury R, Yeoh KK, Tian YM, Hillringhaus L, Bagg EA, Rose NR, Leung IK, Li XS, Woon EC, Yang M, *et al* (2011) The oncometabolite 2-hydroxyglutarate inhibits histone lysine demethylases. *EMBO Rep* 12: 463–9

Cleven AHG, Suijker J, Agrogiannis G, Briaire-de Bruijn IH, Frizzell N, Hoekstra AS, Wijers-Koster PM, Cleton-Jansen A-M & Bovée JVMG (2017) IDH1 or -2 mutations do not predict outcome and do not cause loss of 5-hydroxymethylcytosine or altered histone modifications in central chondrosarcomas. *Clin Sarcoma Res* 7: 8

Cossi M, Rega N, Scalmani G & Barone V (2003) Energies, structures, and electronic properties of molecules in solution with the C-PCM solvation model. *J Comput Chem* 24: 669–681

Dang L, White DW, Gross S, Bennett BD, Bittinger MA, Driggers EM, Fantin VR, Jang HG, Jin S, Keenan MC, *et al* (2009) Cancer-associated IDH1 mutations produce 2-hydroxyglutarate. *Nature* 462: 739–744

Dang L, Yen K & Attar EC (2016) IDH mutations in cancer and progress toward development of targeted therapeutics. *Ann Oncol* 27: 599–608

Dunning TH Jr (1989) Gaussian basis sets for use in correlated molecular calculations. I. The atoms boron through neon and hydrogen. *J Chem Phys* 90: 1007–1023

Emsley P & Cowtan K (2004) Coot: model-building tools for molecular graphics. *Acta Crystallogr D Biol Crystallogr* 60: 2126–32

Emsley P, Lohkamp B, Scott WG & Cowtan K (2010) Features and development of Coot. *Acta Crystallogr D Biol Crystallogr* 66: 486–501

Farrell HM Jr, Deeney JT, Hild EK & Kumosinski TF (1990) Stopped flow and steady state kinetic studies of the effects of metabolites on the soluble form of NADP+:isocitrate dehydrogenase. *J Biol Chem* 265: 17637–43

Figueroa ME, Abdel-Wahab O, Lu C, Ward PS, Patel J, Shih A, Li Y, Bhagwat N, Vasanthakumar A, Fernandez HF, *et al* (2010) Leukemic IDH1 and IDH2 mutations result in a hypermethylation phenotype, disrupt TET2 function, and impair hematopoietic differentiation. *Cancer Cell* 18: 553–67

Frisch MJ, Trucks GW, Schlegel HB, Scuseria GE, Robb MA, Cheeseman JR, Scalmani G, Barone V, Petersson GA, Nakatsuji H, *et al* (2016) Gaussian 16 Rev. C.01.

Gao J, Aksoy BA, Dogrusoz U, Dresdner G, Gross B, Sumer SO, Sun Y, Jacobsen A, Sinha R, Larsson E, *et al* (2013) Integrative analysis of complex cancer genomics and clinical profiles using the cBioPortal. *Sci Signal* 6: pl1

Grimme S, Antony J, Ehrlich S & Krieg H (2010) A consistent and accurate ab initio parametrization of density functional dispersion correction (DFT-D) for the 94 elements H-Pu. *J Chem Phys* 132: 154104

Grimme S, Ehrlich S & Goerigk L (2011) Effect of the damping function in dispersion corrected density functional theory. *J Comput Chem* 32: 1456–1465

Hammes-Schiffer S (2006) Hydrogen tunneling and protein motion in enzyme reactions. *Acc Chem Res* 39: 93–100

Herold RA, Reinbold R, Schofield CJ & Armstrong FA (2023) NADP(H)-dependent biocatalysis without adding NADP(H). *Proc Natl Acad Sci U S A* 120: e2214123120

Hirata M, Sasaki M, Cairns RA, Inoue S, Puviindran V, Li WY, Snow BE, Jones LD, Wei Q, Sato S, *et al* (2015) Mutant IDH is sufficient to initiate enchondromatosis in mice. *Proc Natl Acad Sci U S A* 112: 2829–34

Hohenberg P & Kohn W (1964) Inhomogeneous Electron Gas. *Phys Rev* 136: B864–B871

Jensen F (2001) Polarization consistent basis sets: Principles. *J Chem Phys* 115: 9113–9125

Jensen F (2002) Polarization consistent basis sets. III. The importance of diffuse functions. *J Chem Phys* 117: 9234–9240

Jensen F & Helgaker T (2004) Polarization consistent basis sets. V. The elements Si-Cl. *J Chem Phys* 121: 3463–70

Jurcik A, Bednar D, Byska J, Marques SM, Furmanova K, Daniel L, Kokkonen P, Brezovsky J, Strnad O, Stourac J, *et al* (2018) CAVER Analyst 2.0: analysis and visualization of channels and tunnels in protein structures and molecular dynamics trajectories. *Bioinformatics* 34: 3586–3588

Kabsch W (2010) XDS. *Acta Crystallogr D Biol Crystallogr* 66: 125–132

Leonardi R, Subramanian C, Jackowski S & Rock CO (2012) Cancer-associated isocitrate dehydrogenase mutations inactivate NADPH-dependent reductive carboxylation. *J Biol Chem* 287: 14615–20

Liebschner D, Afonine PV, Baker ML, Bunkóczi G, Chen VB, Croll TI, Hintze B, Hung L-W, Jain S, McCoy AJ, *et al* (2019) Macromolecular structure determination using X-rays, neutrons and electrons: recent developments in ıt Phenix. *Acta Crystallographica Section D* 75: 861–877

Lin J, Lu W, Caravella JA, Campbell AM, Diebold RB, Ericsson A, Fritzen E, Gustafson GR, Lancia DRJ, Shelekhin T, *et al* (2019) Discovery and optimization of quinolinone derivatives as potent, selective, and orally bioavailable mutant isocitrate dehydrogenase 1 (mIDH1) inhibitors. *J Med Chem* 62: 6575–6596

Liu S, Abboud MI, John T, Mikhailov V, Hvinden I, Walsby-Tickle J, Liu X, Pettinati I, Cadoux-Hudson T, McCullagh JSO, *et al* (2021) Roles of metal ions in the selective inhibition of oncogenic variants of isocitrate dehydrogenase 1. *Communications Biology* 4: 1243

Lumpkin RJ & Komives EA (2019) DECA, a comprehensive, automatic post-processing program for HDX-MS data. *Mol Cell Proteomics* 18: 2516–2523

Mardis ER, Ding L, Dooling DJ, Larson DE, McLellan MD, Chen K, Koboldt DC, Fulton RS, Delehaunty KD, McGrath SD, *et al* (2009) Recurring mutations found by sequencing an acute myeloid leukemia genome. *N Engl J Med* 361: 1058–66

Meijers R & Cedergren-Zeppezauer E (2009) A variety of electrostatic interactions and adducts can activate NAD(P) cofactors for hydride transfer. *Chem Biol Interact* 178: 24–28

Paidimuddala B, Mohapatra SB, Gummadi SN & Manoj N (2018) Crystal structure of yeast xylose reductase in complex with a novel NADP-DTT adduct provides insights into substrate recognition and catalysis. *FEBS J* 285: 4445–4464

Patel SM, Smith TG, Morton M, Stiers KM, Seravalli J, Mayclin SJ, Edwards TE, Tanner JJ & Becker DF (2020) Cautionary tale of using tris(alkyl)phosphine reducing agents with NAD+-dependent enzymes. *Biochemistry* 59: 3285–3289

Pavelka A, Sebestova E, Kozlikova B, Brezovsky J, Sochor J & Damborsky J (2016) CAVER: Algorithms for analyzing dynamics of tunnels in macromolecules. *IEEE/ACM Trans Comput Biol Bioinform* 13: 505–517

Peacock RB, Davis JR, Markwick PRL & Komives EA (2018) Dynamic consequences of mutation of tryptophan 215 in thrombin. *Biochemistry* 57: 2694–2703

Pietrak B, Zhao H, Qi H, Quinn C, Gao E, Boyer JG, Concha N, Brown K, Duraiswami C, Wooster R, *et al* (2011) A tale of two subunits: how the neomorphic R132H IDH1 mutation enhances production of alphaHG. *Biochemistry* 50: 4804–12

Plapp BV & Ramaswamy S (2012) Atomic-resolution structures of horse liver alcohol dehydrogenase with NAD(+) and fluoroalcohols define strained Michaelis complexes. *Biochemistry* 51: 4035–4048

Pritchard BP, Altarawy D, Didier B, Gibson TD & Windus TL (2019) New Basis Set Exchange: An Open, Up-to-Date Resource for the Molecular Sciences Community. *J Chem Inf Model* 59: 4814–4820

Pusch S, Schweizer L, Beck AC, Lehmler JM, Weissert S, Balss J, Miller AK & von Deimling A (2014) D-2-Hydroxyglutarate producing neo-enzymatic activity inversely correlates with frequency of the type of isocitrate dehydrogenase 1 mutations found in glioma. *Acta Neuropathol Commun* 2: 19

Ramsey KM, Dembinski HE, Chen W, Ricci CG & Komives EA (2017) DNA and IκBα both induce long-range conformational changes in NFκB. *J Mol Biol* 429: 999–1008

Rendina AR, Pietrak B, Smallwood A, Zhao H, Qi H, Quinn C, Adams ND, Concha N, Duraiswami C, Thrall SH, *et al* (2013) Mutant IDH1 enhances the production of 2-hydroxyglutarate due to its kinetic mechanism. *Biochemistry* 52: 4563–77

Roman JV, Melkonian TR, Silvaggi NR & Moran GR (2019) Transient-state analysis of human isocitrate dehydrogenase I: accounting for the interconversion of active and non-active conformational states. *Biochemistry* 58: 5366–5380

Sabo KA, Albekioni E, Caliger D, Coleman NJ, Thornberg E, Avellaneda Matteo D, Komives EA, Silletti S & Sohl CD (2023) Capturing the dynamic conformational changes of human isocitrate dehydrogenase 1 (IDH1) upon ligand and metal binding using hydrogen-deuterium exchange mass spectrometry. *Biochemistry* 62: 1145–1159

Sanli G, Dudley JI & Blaber M (2003) Structural biology of the aldo-keto reductase family of enzymes: catalysis and cofactor binding. *Cell Biochem Biophys* 38: 79–101

Schrödinger, LLC. The PyMOL Molecular Graphics System, Version 2.5.2

Seery VL & Farrell HMJ (1990) Spectroscopic evidence for ligand-induced conformational change in NADP+:isocitrate dehydrogenase. *J Biol Chem* 265: 17644–17648

Sharma N, Mallela AN, Shi DD, Tang LW, Abou-Al-Shaar H, Gersey ZC, Zhang X, McBrayer SK & Abdullah KG (2023) Isocitrate dehydrogenase mutations in gliomas: A review of current understanding and trials. *Neurooncol Adv* 5: vdad053

Simon S, Duran M & Dannenberg JJ (1996) How does basis set superposition error change the potential surfaces for hydrogen-bonded dimers? *J Chem Phys* 105: 11024–11031

Tangella AV, Gajre A & Kantheti VV (2023) Isocitrate dehydrogenase 1 mutation and ivosidenib in patients with acute myeloid leukemia: a comprehensive review. *Cureus* 15: e44802

Wales TE, Fadgen KE, Gerhardt GC & Engen JR (2008) High-speed and high-resolution UPLC separation at zero degrees Celsius. *Anal Chem* 80: 6815–6820

Wilson AK, van Mourik T & Dunning TH (1996) Gaussian basis sets for use in correlated molecular calculations. VI. Sextuple zeta correlation consistent basis sets for boron through neon. *J Mol Struct* 388: 339–349

Xie X, Baird D, Bowen K, Capka V, Chen J, Chenail G, Cho Y, Dooley J, Farsidjani A, Fortin P, *et al* (2017) Allosteric mutant IDH1 inhibitors reveal mechanisms for IDH1 mutant and isoform selectivity. *Structure* 25: 506–513

Xu X, Zhao J, Xu Z, Peng B, Huang Q, Arnold E & Ding J (2004) Structures of human cytosolic NADP-dependent isocitrate dehydrogenase reveal a novel self-regulatory mechanism of activity. *J Biol Chem* 279: 33946–57

Yan H, Parsons DW, Jin G, McLendon R, Rasheed BA, Yuan W, Kos I, Batinic-Haberle I, Jones S, Riggins GJ, *et al* (2009) IDH1 and IDH2 mutations in gliomas. *N Engl J Med* 360: 765–73

Yang B, Zhong C, Peng Y, Lai Z & Ding J (2010) Molecular mechanisms of ‘off-on switch’ of activities of human IDH1 by tumor-associated mutation R132H. *Cell Res* 20: 1188–200

Zhao Y & Truhlar DG (2008) The M06 suite of density functionals for main group thermochemistry, thermochemical kinetics, noncovalent interactions, excited states, and transition elements: two new functionals and systematic testing of four M06-class functionals and 12 other functionals. *Theor Chem Acc* 120: 215–241